E1-2008-108

V. V. Lyubushkin[1], B. A. Popov[2]

A STUDY OF QUASI-ELASTIC MUON (ANTI)NEUTRINO SCATTERING IN THE NOMAD EXPERIMENT

[1]E-mail: Vladimir.Lyubushkin@cern.ch
[2]E-mail: Boris.Popov@cern.ch

Любушкин В. В., Попов Б. А. E1-2008-108
Изучение квазиупругого рассеяния мюонного (анти)нейтрино
в эксперименте NOMAD

Данная работа посвящена изучению процессов квазиупругого рассеяния мюонных нейтрино и антинейтрино ($\nu_\mu n \to \mu^- p$ и $\bar{\nu}_\mu p \to \mu^+ n$) в эксперименте NOMAD. Измерение сечений данных процессов на ядерной мишени (преимущественно углероде) выполнено посредством нормировки на полное сечение взаимодействия ν_μ ($\bar{\nu}_\mu$) по каналу заряженного тока. Для сечений нейтрино и антинейтрино, усредненных по спектру в интервале энергий 3–100 ГэВ, получены следующие результаты: $\langle\sigma_{\rm qel}\rangle_{\nu_\mu} = (0{,}92 \pm 0{,}02$ (стат.) $\pm\, 0{,}06$ (сист.)$) \cdot 10^{-38}$ см^2 и $\langle\sigma_{\rm qel}\rangle_{\bar{\nu}_\mu} = (0{,}81 \pm 0{,}05$ (стат.) $\pm\, 0{,}08$ (сист.)$) \cdot 10^{-38}$ см^2. Значение аксиальной массы нуклона M_A, соответствующее $\langle\sigma_{\rm qel}\rangle_{\nu_\mu}$, равно $M_A = 1{,}05 \pm 0{,}02$ (стат.) $\pm\, 0{,}06$ (сист.) ГэВ. Оно находится в хорошем согласии с величиной M_A, вычисленной для сечения квазиупругого рассеяния антинейтрино, и не противоречит данным, полученным из анализа Q^2-распределения, но обладает наименьшей систематической ошибкой. Найденное значение M_A хорошо согласуется с усредненным результатом предыдущих измерений. Недавно опубликованные измерения M_A в экспериментах K2K и MiniBooNE несколько отличаются от нашего значения, хотя формально и не противоречат ему ввиду их больших ошибок.

Работа выполнена в Лаборатории ядерных проблем им. В. П. Джелепова ОИЯИ.

Сообщение Объединенного института ядерных исследований. Дубна, 2008

Lyubushkin V. V., Popov B. A. E1-2008-108
A Study of Quasi-Elastic Muon (Anti)Neutrino Scattering
in the NOMAD Experiment

We have studied the muon neutrino and antineutrino quasi-elastic (QEL) scattering reactions ($\nu_\mu n \to \mu^- p$ and $\bar{\nu}_\mu p \to \mu^+ n$) using a set of experimental data collected by the NOMAD collaboration. We have performed measurements of the cross section of these processes on a nuclear target (mainly carbon) normalizing it to the total ν_μ ($\bar{\nu}_\mu$) charged current cross section. The results for the flux averaged QEL cross sections in the (anti)neutrino energy interval 3–100 GeV are $\langle\sigma_{\rm qel}\rangle_{\nu_\mu} = (0.92 \pm 0.02$ (stat.) $\pm\, 0.06$ (syst.)$) \cdot 10^{-38}$ cm^2 and $\langle\sigma_{\rm qel}\rangle_{\bar{\nu}_\mu} = (0.81 \pm 0.05$ (stat.) $\pm\, 0.08$ (syst.)$) \cdot 10^{-38}$ cm^2 for neutrino and antineutrino, respectively. The axial mass parameter M_A was extracted from the measured quasi-elastic neutrino cross section. The corresponding result is $M_A = 1.05 \pm 0.02$ (stat.) $\pm\, 0.06$ (syst.) GeV. It is consistent with the axial mass values recalculated from the antineutrino cross section and extracted from the pure Q^2 shape analysis of the high purity sample of ν_μ quasi-elastic 2-track events, but has smaller systematic error and should be quoted as the main result of this work. The measured M_A is found to be in good agreement with the world average value obtained in the previous deuterium filled bubble chamber experiments. These results do not support M_A measurements published recently by the K2K and MiniBooNE collaborations, which reported somewhat larger values, which are however compatible with our results within their large errors.

The investigation has been performed at the Dzhelepov Laboratory of Nuclear Problems, JINR.

Communication of the Joint Institute for Nuclear Research. Dubna, 2008

1. INTRODUCTION

A precise knowledge of the cross section of (anti)neutrino–nucleus quasi-elastic scattering process (QEL) is important for the planning and analysis of any experiment which detects astrophysical, atmospheric or accelerator neutrinos. The available measurements from the early experiments at ANL [1–4], BNL [5–8], FNAL [9, 10], CERN [11–18] and IHEP [19–22] have considerable errors due to low statistics and a lack of knowledge of the precise incoming neutrino flux. Unfortunately, even within these large errors, the results are often conflicting.

This subject remains very hot. Recently several attempts have been made to investigate the QEL process in the data collected by modern accelerator neutrino experiments (such as NuTeV [23], K2K [24, 25] and MiniBooNE [26]). Unfortunately, they have not clarified the situation again due to large errors assigned to their measurements. Dedicated experiments, such as, e.g., SciBooNE [27] and MINERνA [28], are now being performed.

In the present analysis, we study both ν_μ and $\bar{\nu}_\mu$ QEL scattering in the data collected by the NOMAD collaboration. The NOMAD detector was exposed to a wide-band neutrino beam produced by the 450 GeV proton synchrotron (SPS, CERN). A detailed description of the experimental set-up can be found in [29]. The characteristics of the incoming neutrino flux are given in [30].

The large amount of collected data and the good quality of event reconstruction in the NOMAD detector provide a unique possibility to measure the QEL cross section with unprecedently small statistical errors. The data sample used in this analysis consists of about 751000 (23000) ν_μ ($\bar{\nu}_\mu$) charged-current (CC) interactions in a reduced detector fiducial volume. The average energy of the incoming ν_μ ($\bar{\nu}_\mu$) is 25.9 (17.6) GeV.

The paper is organized as follows. In Sec. 2 we give a brief review of the published experimental data on QEL (anti)neutrino scattering. The NOMAD detector and the incoming neutrino flux are briefly discussed in Sec. 3. In Sec. 4 we outline the MC modeling of signal and background events, emphasizing also the importance of nuclear effects. Section 5 is devoted to the selection of the QEL events; we describe the QEL identification procedure and compare the MC predictions with experimental data. The methods used to measure the QEL cross section and the phenomenological axial mass parameter M_A are the subjects of

Sec. 6. The systematic uncertainties are summarized in Sec. 7. The results are presented in Sec. 8. Finally, a summary and discussion of the obtained results are given in Sec. 9.

2. REVIEW OF EXISTING EXPERIMENTAL DATA ON QUASI-ELASTIC (ANTI)NEUTRINO SCATTERING

Let us start with a brief review of existing experimental data on (anti)neutrino nucleon QEL scattering.

Figures 1 and 2 show a compilation of available data on the cross-section measurement of the ν_μ quasi-elastic scattering off deuterons (and other nuclei or composite targets like freon, propane, liquid scintillator) as a function of the incoming neutrino energy. In Fig. 3 a similar plot is presented for the case of $\bar{\nu}_\mu$ scattering. From these figures one can conclude that the QEL cross section measured in different experiments can vary by 20–40%.

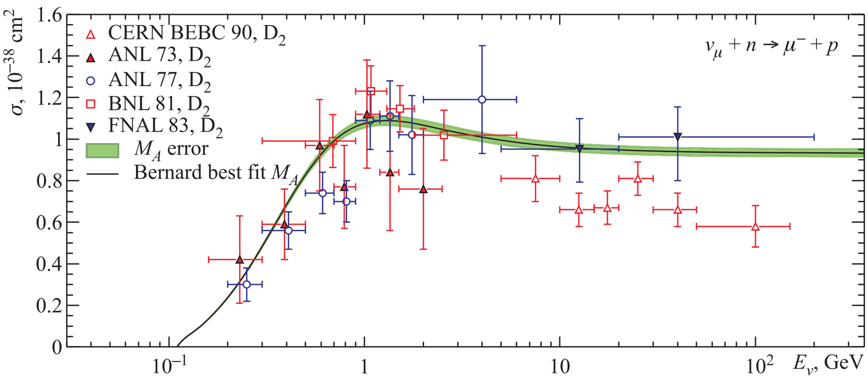

Fig. 1. Total cross section of $\nu_\mu n \to \mu^- p$ process extracted from $\nu_\mu D$ scattering data. The solid curve corresponds to the world average value of axial mass $M_A = 1.026$ GeV while the shaded area shows a ± 0.021 GeV error band. Points correspond to available experimental data from ANL 73 (Argonne 12-foot BC) [2], ANL 77 [3], BNL 81 (Brookhaven 7-foot BC) [6], FNAL 83 (FermiLab 15-foot BC) [9], BEBC 90 (CERN, Big European Bubble Chamber) [18]; corrections for nuclear effects have been made by the authors of the experiments

The existing data on (anti)neutrino QEL scattering come mostly from bubble chamber (BC) experiments. In general, these data suffer from small statistics. Moreover, results of several old experiments [12–14] have large systematic uncertainties due to the poor knowledge of the incoming neutrino flux and of background contamination in the selected events.

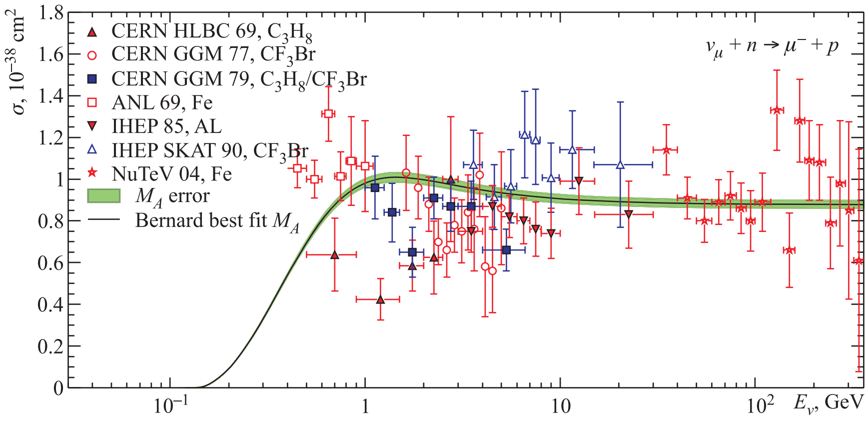

Fig. 2. Total cross section of $\nu_\mu n \to \mu^- p$ process extracted from the data on ν_μ scattering off heavy nuclei. Nuclear effects are included into calculations according to the relativistic Fermi gas model by Smith and Moniz [31] for carbon with binding energy $E_b = 25.6$ MeV and Fermi momentum $P_F = 221$ MeV; the axial mass value is the same as for Fig. 1. Points correspond to available experimental data from ANL 69 (spark-chamber) [1], NuTeV 04 (FermiLab) [23], CERN HLBC 69 (CERN, Heavy Liquid Bubble Chamber) [14], CERN GGM 77 (CERN, Gargamelle BC) [15], CERN GGM 79 [17], IHEP 85 (IHEP, spark-chamber) [20], IHEP SCAT 90 (IHEP, BC) [22]

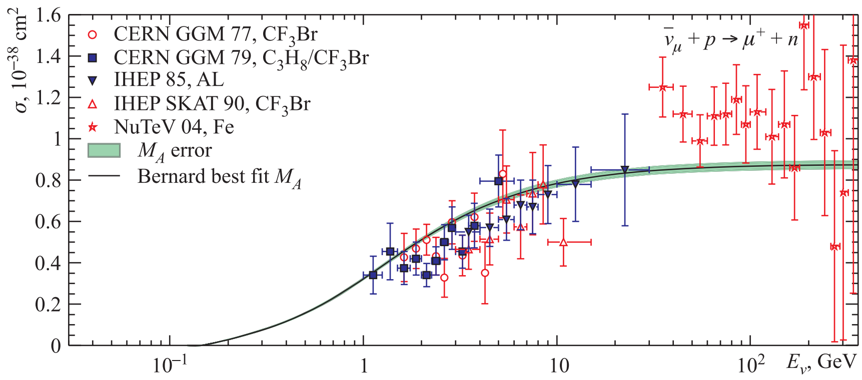

Fig. 3. Total cross section of $\bar{\nu}_\mu p \to \mu^+ n$ process extracted from the data on $\overline{\nu}_\mu$ scattering off heavy nuclei. Nuclear effects are included into calculations according to the relativistic Fermi gas model by Smith and Moniz [31] for carbon; the axial mass value is the same as for Fig. 1. Points correspond to available experimental data from CERN GGM 77 [15], CERN GGM 79 [16], IHEP 85 [20], IHEP SCAT 90 [22] and NuTeV 04 [23]

The total QEL cross section was recently measured in data collected by the NuTeV collaboration [23]. The number of QEL events identified in their analysis are comparable with the total world data obtained in the previous experiments. However, the results reported for the antineutrino case fall well outside the most probable range of values known today and hence, seem to exhibit a systematic shift.

Another intriguing subject in the study of the neutrino quasi-elastic scattering is the axial structure of the nucleon. We will skip here the details of the phenomenology of the hadronic current involved in the matrix element of the process (see Subsec. 4.1). But let us only remind the reader that for the region of low and moderate 4-momentum transfer Q^2, we can use a dipole parametrization for the axial form factor with only one adjustable parameter, the so-called axial mass M_A.

The M_A parameter describes the internal structure of the nucleon and does not depend on the incoming neutrino flux (unlike the measured flux-averaged cross section) and should be the same both for neutrino and antineutrino experiments (if we assume the isotopic invariance of strong interaction). Therefore, it is convenient to compare experimental results in terms of the axial mass.

There are two possible ways generally used to extract the M_A parameter from experimental data:

1) from the total (anti)neutrino nucleon cross section (the axial form factor is responsible for about 50–60% of the total QEL cross section);

2) from the fit of the Q^2 distribution of the identified neutrino QEL events.

In principle, these two procedures should give self-consistent results. However, the old bubble chamber experiments at ANL and CERN reported in general larger values of M_A based on the Q^2 fit than those obtained from the total cross-section measurements.

Results of the M_A measurements published recently by the K2K [24] and MiniBooNE [26] collaborations are about 15% higher than the average of previous deuterium filled bubble chamber experiments. Moreover, they exhibit large systematic errors (in spite of large numbers of collected events).

Let us note that the extraction of M_A from the Q^2 distribution fit is a more delicate issue than the QEL total cross-section measurement.

There are at least three aspects which can affect noticeably the final result:

1) The nuclear effects can distort the expected distributions of the measured kinematic variables (like the energy of the outgoing nucleon). The neutrino–nucleus interactions should be described by a theoretical model suitable for the considered neutrino energy region. This is important both for MC modeling in

Table 1. A summary of existing experimental data: the axial mass M_A as measured in the previous neutrino experiments. Numbers of observed events have been taken from the original papers; usually they are not corrected for efficiency and purity (the so-called QEL candidates). The axial mass value for the NuTeV experiment [23] was estimated from the published neutrino quasi-elastic cross section ($\langle\sigma_{\rm qel}\rangle_\nu = (0.94 \pm 0.03$ (stat.) ± 0.07 (syst.)$) \cdot 10^{-38}$ cm^2); systematic error for IHEP SKAT 90 [22] is 0.14 GeV

Experiment	Target	Events	Method	M_A, GeV	Ref.
ANL 69	Steel		$d\sigma/dQ^2$	1.05 ± 0.20	[1]
			σ	0.97 ± 0.16	
ANL 73	Deuterium	166	$d\sigma/dQ^2$	0.94 ± 0.18	[2]
			$\sigma \otimes d\sigma/dQ^2$	0.95 ± 0.12	
			σ	$0.75^{+0.13}_{-0.11}$	
ANL 77	Deuterium	~ 600	$d\sigma/dQ^2$	1.01 ± 0.09	[3]
			$\sigma \otimes d\sigma/dQ^2$	0.95 ± 0.09	
			σ	0.74 ± 0.12	
ANL 82	Deuterium	1737	$d\sigma/dQ^2$	1.05 ± 0.05	[6]
			$\sigma \otimes d\sigma/dQ^2$	1.03 ± 0.05	
BNL 81	Deuterium	1138	$d\sigma/dQ^2$	1.07 ± 0.06	[4]
BNL 90	Deuterium	2538	$d\sigma/dQ^2$	$1.070^{+0.040}_{-0.045}$	[8]
FermiLab 83	Deuterium	362	$d\sigma/dQ^2$	$1.05^{+0.12}_{-0.16}$	[9]
NuTeV 04	Steel	21614	σ	1.11 ± 0.08	[23]
MiniBooNE 07	Mineral oil	193709	$d\sigma/dQ^2$	1.23 ± 0.20	[26]
CERN HLBC 64	Freon	236	$d\sigma/dQ^2$	$1.00^{+0.35}_{-0.20}$	[11]
CERN HLBC 67	Freon			$0.75^{+0.24}_{-0.20}$	[12]
CERN SC 68	Steel			$0.65^{+0.45}_{-0.40}$	[13]
CERN HLBC 69	Propane	130		0.70 ± 0.20	[14]
			$d\sigma/dQ^2$	0.88 ± 0.19	
CERN GGM 77	Freon	687	σ	0.96 ± 0.16	[15]
			$d\sigma/dQ^2$	0.87 ± 0.18	
CERN GGM 79	Propane/Freon	556	σ	0.99 ± 0.12	[17]
			$d\sigma/dQ^2$	0.94 ± 0.07	
CERN BEBC 90	Deuterium	552	σ	1.08 ± 0.08	[18]
IHEP 82	Aluminium	898	$d\sigma/dQ^2$	1.00 ± 0.07	[19]
IHEP 85	Aluminium	1753	$d\sigma_{\nu+\bar\nu}/dQ^2$	1.00 ± 0.04	[20]
IHEP SCAT 88	Freon	464	$\sigma \otimes d\sigma/dQ^2$	0.96 ± 0.15	[21]
			σ	1.08 ± 0.07	
IHEP SCAT 90	Freon		$d\sigma/dQ^2$	1.05 ± 0.07	[22]
			$\sigma \otimes d\sigma/dQ^2$	1.06 ± 0.05	
K2K 06, SciFi	Water		$d\sigma/dQ^2$	1.20 ± 0.12	[24]
K2K 08, SciBar	Carbon		$d\sigma/dQ^2$	1.144 ± 0.077	[25]

present-day neutrino experiments and for a proper interpretation of the results obtained earlier (with few exceptions for the deuterium filled bubble chambers).

2) The correct determination of the background contamination from both deep inelastic scattering and single pion production in the selected events is im-

Table 2. The same as in Table 1, but for antineutrino experiments. The axial mass value for the NuTeV experiment [23] was estimated from the published antineutrino quasi-elastic cross section ($\sigma_{\bar{\nu}}^{\rm qel} = (1.12 \pm 0.04$ (stat.) $\pm\, 0.10$ (syst.)$) \cdot 10^{-38}$ cm^2); systematic error for IHEP SKAT 90 [22] is 0.20 GeV

Experiment	Target	Events	Determined from	M_A, GeV	Ref.
BNL 80	Hydrogen		$d\sigma/dQ^2$	$0.9^{+0.4}_{-0.3}$	[5]
BNL 88	Liquid scint.	2919	$d\sigma/dQ^2$	1.09 ± 0.04	[7]
FermiLab 84	Neon	405	$d\sigma/dQ^2$	0.99 ± 0.11	[10]
NuTeV 04	Steel	15054	σ	1.29 ± 0.11	[23]
			σ	0.69 ± 0.44	
CERN GGM 77	Freon	476	$d\sigma/dQ^2$	0.94 ± 0.17	[15]
			σ	$0.84^{+0.08}_{-0.09}$	
CERN GGM 79	Propane/Freon	766	$d\sigma/dQ^2$	0.91 ± 0.04	[16]
IHEP 85	Aluminium	854	$d\sigma_{\nu+\bar{\nu}}/dQ^2$	1.00 ± 0.04	[20]
IHEP SKAT 88	Freon	52	$\sigma \otimes d\sigma/dQ^2$	0.72 ± 0.23	[21]
			σ	0.62 ± 0.16	
IHEP SKAT 90	Freon		$d\sigma/dQ^2$	0.79 ± 0.11	[22]
			$\sigma \otimes d\sigma/dQ^2$	0.71 ± 0.10	

portant for experiments operating with intermediate and high energy neutrino beams. The (over) underestimation of this background should lead to an effectively (smaller) larger value of the measured total QEL cross section, whereas the result for M_A obtained from a fit of the Q^2 distribution becomes unpredictable.

3) The QEL reconstruction efficiency as a function of Q^2 is not expected to be a flat function. It should drop both at small Q^2 due to the loss of low energy protons and at large Q^2 due to the loss of low energy muons. Effects which influence the efficiency of the low momentum particle reconstruction should be carefully taken into account in the MC modeling of the detector response.

In Fig. 4 we present the world compilation of M_A measurements from neutrino (left panel) and antineutrino (right panel) experiments. Tables 1 and 2 display the measured values of M_A from the same data. Whenever possible we provide also the M_A measured from the total cross section.

From the tables and plots above one can conclude that the presently available experimental data on the neutrino QEL cross section allow for a very wide spread of the axial mass values, roughly from 0.7 to 1.3 GeV. Therefore the reliability of a theoretical fit to these data is questionable and the uncertainty attributed to such a fit should go beyond the averaged experimental statistical accuracy. Nevertheless, the formal averaging of M_A values from several early experiments was done by the authors of [32]: $M_A = 1.026 \pm 0.021$ GeV. This result is also known as the

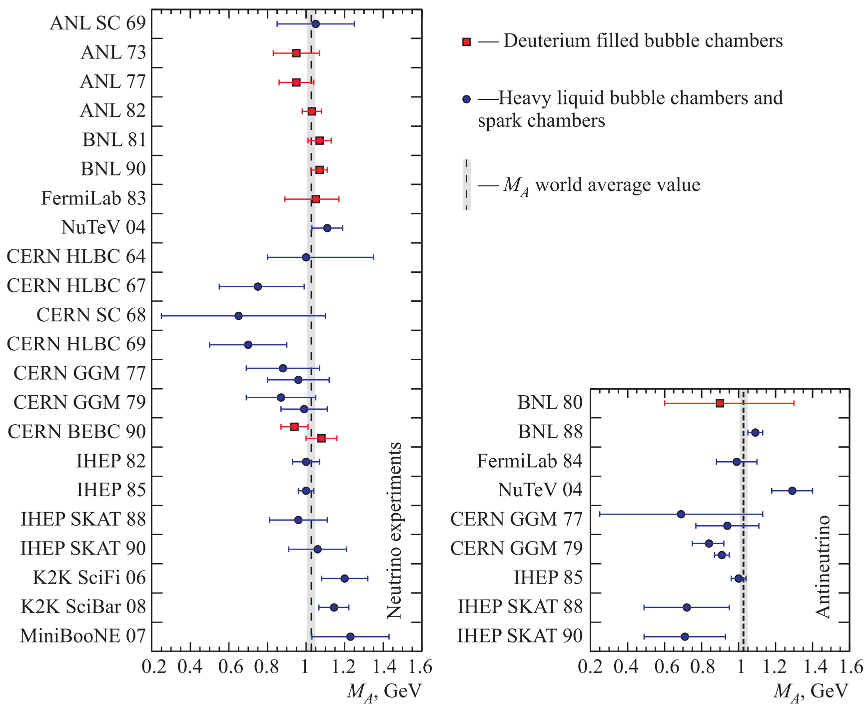

Fig. 4. A summary of existing experimental data: the axial mass M_A as measured in the previous neutrino (left) and antineutrino (right) experiments. Points show results obtained both from deuterium filled BC (squares) and from heavy liquid BC and spark chambers (circles). Dashed line corresponds to the so-called world average value $M_A = 1.026 \pm 0.021$ GeV (see [32])

axial mass world average value. According to [33–35] an updated world average value from pion electroproduction experiments is $M_A = 1.014 \pm 0.016$ GeV.

3. THE NOMAD DETECTOR

The NOMAD detector [29] consisted of an active target of 44 drift chambers with a total fiducial mass of 2.7 t, located in a 0.4 T dipole magnetic field as shown in Fig. 5. The $X \times Y \times Z$ total volume of the drift chambers is about $300 \times 300 \times 400$ cm^3.

Drift chambers [36], made of low Z material served the dual role of a nearly isoscalar target* for neutrino interactions and of tracking medium. The average density of the drift chamber volume was $0.1\ \mathrm{g/cm^3}$. These chambers provided an overall efficiency for charged track reconstruction of better than 95% and a momentum resolution which can be approximated by the following formula: $\frac{\sigma_p}{p} \approx \frac{0.05}{\sqrt{L}} \oplus \frac{0.008p}{\sqrt{L^5}}$, where the momentum p is in GeV/c and the track length L is in m. Reconstructed tracks were used to determine the event topology (the assignment of tracks to vertices), to reconstruct the vertex position and the track parameters at each vertex and, finally, to identify the vertex type (primary, secondary, etc.). A transition radiation detector [37, 38] placed at the end of the active target was used for particle identification. A lead-glass electromagnetic calorimeter [39, 40] located downstream of the tracking region provided an energy resolution of $3.2\%/\sqrt{E[\mathrm{GeV}]} \oplus 1\%$ for electromagnetic showers and was crucial to measure the total energy flow in neutrino interactions. In addition, an iron absorber and a set of muon chambers located after the electromagnetic calorimeter was used for muon identification, providing a muon detection efficiency of 97% for momenta greater than 5 GeV/c.

The NOMAD neutrino beam consisted mainly of ν_μ's with an about 7% admixture of $\bar{\nu}_\mu$ and less than 1% of ν_e and $\bar{\nu}_e$. More details on the beam composition can be found in [30].

The main goal of the NOMAD experiment was the search for neutrino oscillations in a wide band neutrino beam from the CERN SPS [41, 42]. A very good quality of event reconstruction similar to that of bubble chamber experiments and a large data sample collected during four years of data taking (1995–1998) allow for detailed studies of neutrino interactions.

4. MONTE CARLO SIMULATION OF NEUTRINO INTERACTIONS

Inclusive (anti)neutrino charged current (CC) and neutral current (NC) scatterings can be considered as a mixture of several processes described by significantly different models. In our case, these are quasi-elastic scattering (QEL), single-pion production (RES) and deep inelastic scattering (DIS). Below we will describe in detail the simulation scheme used for each of these processes and discuss the influence of the nuclear effects.

An adequate MC description of neutrino interactions is important to calculate the efficiency of the QEL selection. Moreover, it allows us to predict the level

*The NOMAD active target is nearly isoscalar ($n_n : n_p = 47.56\% : 52.43\%$) and consists mainly of carbon; a detailed description of the drift chamber composition can be found in [36].

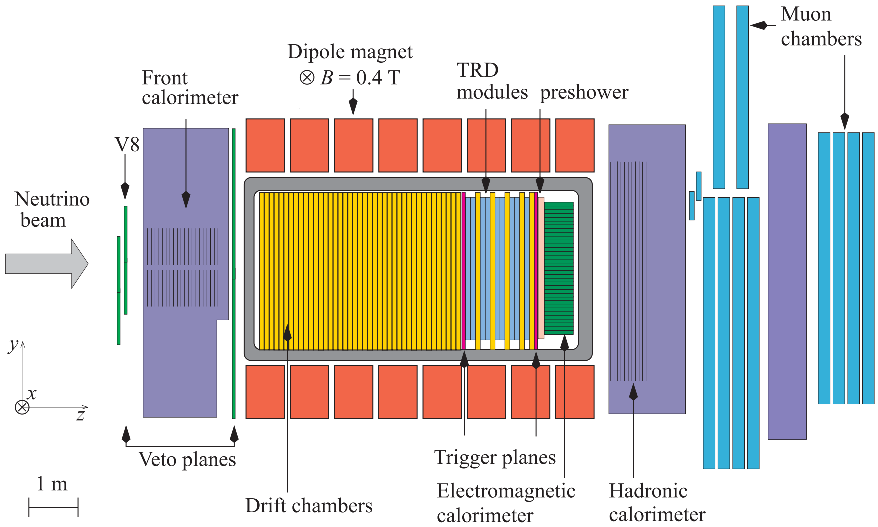

Fig. 5. A side-view of the NOMAD detector

of background, which cannot be suppressed completely by the QEL identification scheme proposed in Sec. 5.

4.1. Quasi-Elastic Neutrino Scattering. The standard representation of the weak hadronic current involved in the matrix elements of the processes $\nu_\mu n \to \mu^- p$ and $\overline{\nu}_\mu p \to \mu^+ n$, is expressed in terms of 6 form factors, which in general are assumed to be complex [43]. They formally describe the hadronic structure and cannot be calculated analytically within the framework of the electroweak interaction theory.

We neglect the second-class current contributions associated with the scalar and pseudo-tensor form factors. This is equivalent to the requirement of time reversal invariance of the matrix element (hence all form factors should be real functions of Q^2) and charge symmetry of the hadronic current (rotation about the second axis in the isotopic space).

The vector form factors F_V and F_M are related through the hypothesis of isotopic invarince to the electromagnetic ones, which we will consider to be well known. Instead of the simple dipole parametrization, extensively used in the previous experiments, we have chosen the Gari–Krüempelmann (GK) model [44] extended and fine-tuned by Lomon [45]. Specifically we explore the «GKex(05)» set of parameters [46] which fits the modern and consistent older data well and meets the requirements of dispersion relations and of QCD at low and high 4-momentum transfer [44].

For the axial and pseudoscalar form factors we use the conventional representations [43]:

$$F_A\left(Q^2\right) = F_A(0)\left(1+\frac{Q^2}{M_A^2}\right)^{-2} \tag{1}$$

and

$$F_P\left(Q^2\right) = \frac{2m_N^2}{m_\pi^2+Q^2}F_A\left(Q^2\right), \tag{2}$$

where $F_A(0) = g_A = -1.2695 \pm 0.0029$ (measured in neutron β-decay [47]); m_π and m_N — pion and nucleon masses.

As discussed in Sec. 2, the currently available experimental data on the axial mass M_A allow for a wide spread. Thus, in our case, it should be considered as one of the available parameters, which can be used to adjust the MC simulation with the measured value of the total QEL cross section and observed distributions of the kinematic variables (other parameters, related to the modeling of the intranuclear cascade, will be described later).

Note that the expression for the pseudoscalar form factor F_P is nothing better than a plausible parametrization inspired by the PCAC hypothesis and the assumption that the pion pole dominates at $Q^2 \lesssim m_\pi^2$ [43]. However, its contribution enters into the cross sections multiplied by a factor $(m_\mu/m_N)^2$. Hence, the importance of the related uncertainty is much diminished.

4.2. Single-Pion Production Through Intermediate Baryon Resonances. In order to describe the single-pion neutrino production through baryon resonances we adopt an extended version of the Rein and Sehgal model (RS) [48,49], which seems to be one of the most widely trusted phenomenological approaches for calculating the RES cross sections. The generalization proposed in [50,51] takes into account the final lepton mass and is based upon a covariant form of the charged leptonic current with definite lepton helicity. In our MC simulation we use the same set of 18 interfering nucleon resonances with masses below 2 GeV as in [48] but with all relevant input parameters updated according to the current data [47]. Significant factors (normalization coefficients, etc.), estimated in Ref. [48] numerically are recalculated by using the new data and a more accurate integration algorithm.

The relativistic quark model of Feynman, Kislinger, and Ravndal [52], adopted in the RS approach, unambiguously determines the structure of the transition amplitudes involved into the calculation and the only unknown structures are the vector and axial-vector transition form factors $G^{V,A}(Q^2)$. In [48] they are assumed to have the form

$$\frac{G^{V,A}(Q^2)}{G^{V,A}(0)} = \left(1+\frac{Q^2}{4m_N^2}\right)^{1/2-n}\left(1+\frac{Q^2}{M_{V,A}^2}\right)^{-2}, \tag{3}$$

where the integer n in the first (ad hoc) factor in Eq. (3) is the number of oscillation quanta of the intermediate resonance.

The vector mass M_V is taken to be 0.84 GeV, that is the same as in the usual dipole parametrization of the nucleon electromagnetic form factors. The axial mass (which was fixed at 0.95 GeV in the original RS paper) is set to the standard world averaged value $M_A = 1.03$ GeV. It is in good agreement with the results obtained in the recent analysis of the data from the BNL 7-foot deuterium filled bubble chamber [53] ($M_A = 1.08 \pm 0.07$ GeV). Let us also note that the available experimental data for the single-pion neutrino production (as in the case of QEL scattering) does not permit a very definite conclusion about the value of the total RES cross section (and the corresponding axial mass value). The present uncertainties will be taken into account in the calculation of the systematic error of the current analysis.

To compensate for the difference between the SU_6 predicted value $(-5/3)$ and the experimental value for the nucleon axial-vector coupling g_A, Rein and Sehgal introduced a renormalization factor $Z = 0.75$. In order to adjust the renormalization to the current world averaged value $g_A = -1.2695$ [47] we have adopted $Z = 0.762$. The harmonic-oscillator constant Ω, which accounts for the mass differences between states with different numbers of excitation quanta is set to its original value $\Omega = 1.05$ GeV^2.

Another essential ingredient of the RS approach is the nonresonant background (NRB). Its contribution is important in describing the existing data on the reactions $\nu_\mu n \to \mu^- n\pi^+$, $\nu_\mu n \to \mu^- p\pi^0$, $\bar{\nu}_\mu p \to \mu^+ p\pi^-$ and $\bar{\nu}_\mu p \to \mu^+ n\pi^0$. In our Monte Carlo, the NRB is taken to come from the DIS part of the simulation. Therefore it has not been used in the RES part of our event generator.

4.3. Deep Inelastic Scattering. The MC simulation of the deep inelastic neutrino nucleon scattering is based on the LEPTO 6.5.1 package [55] with several modifications [56, 57]. For hadronization we use the LUND string fragmentation model, as incorporated into the JETSET 7.4 program [58–60].

Upon implementing the Monte Carlo for $\nu_\mu(\bar{\nu}_\mu)$ CC scattering, kinematic boundaries between exclusive (RES) and inclusive (DIS) channels must be defined. To avoid double counting, the phase space of the RES and DIS contributions should be separated by the conditions $W < W_{\rm cut}^{\rm RES}$ and $W > W_{\rm cut}^{\rm DIS}$, where W is the invariant mass of the final hadronic system.

The maximum possible value for $W_{\rm cut}^{\rm RES}$ is the upper limit of the RS model (2 GeV), while inelastic scattering can take place from the two-pion production threshold $W_{2\pi} = m_N + 2m_\pi \simeq 1.2$ GeV (however, this value is too small in principle since the structure functions used in the calculation of the DIS cross section cannot be extrapolated down to $W_{2\pi}$).

Additional constraints could likely be obtained from the concept of quark–hadron duality, which is based on the idea that DIS structure functions describe on average the data in the resonance region [61]. However, whether conclusions valid for electron–nucleon scattering should hold for the axial part of the hadronic current is not clear. For example, recent theoretical investigations made specifically for the RS model predict the absence of duality in neutrino scattering off isoscalar targets [62].

So, there is no clear physical recipe to determine exact numerical values for those cutoff parameters. The authors of GENIE MC code [63] adopt the value $W_{\rm cut}^{\rm RES} \simeq W_{\rm cut}^{\rm DIS} \sim 1.7$ GeV. A comprehensive analysis of available experimental data made in [54, 64] suggests to decrease this cut to ~ 1.5 GeV.

In the present analysis we set $W_{\rm cut}^{\rm RES} = 2$ GeV and $W_{\rm cut}^{\rm DIS} = 1.4$ GeV. This choice allows for the nonresonant contribution to single-pion production to be accounted for by the DIS part of the Monte Carlo (see the previous Section). Moreover, it is not at variance with experimental data as far as the total (anti)neutrino cross section is concerned (see Fig. 6).

4.4. Coherent Pion Production. In the processes described above, neutrinos interact with individual target nucleons. However, pions can be produced in a coherent interaction of the neutrino with the whole nucleus, i.e., in the case of CC ν_μ scattering $\nu_\mu\,\mathcal{N} \to \mu^-\pi^+\mathcal{N}$, where $\mathcal{N}$ is the target nucleus.

The details of the MC simulation can be found in [65], which is devoted to the investigation of this process in the NOMAD experiment. The flux averaged cross section has been calculated following [66, 67] and has been estimated at $0.733\cdot 10^{-38}$ cm^2 per nucleus. Taking into account that the average mass number of the NOMAD target is 12.9, and using the number of registered DIS events (see Subsec. 6.1) one finds that the expected number of coherent pion production events is ~ 2700. Nevertheless, the probability for events of this type to be identified as QEL is $\sim 2\%$ because of the small pion emission angle, so that the expected contamination of the selected QEL sample is lower than 0.4%.

4.5. Nuclear Effects. For typical NOMAD neutrino energies, we can assume that the incident neutrino interacts with one nucleon only inside the target nucleus, while the remaining nucleons are spectators (Impulse Approximation). In this case, one can describe the neutrino nucleus scattering by folding the usual expressions for the free neutrino nucleon cross sections with a Fermi gas distribution.

In the relativistic Fermi gas model, the nucleus is considered as an infinite system of noninteracting nucleons. The phenomena related to the nuclear surface and to the interaction between nucleons can be taken into account by using a more realistic effective momentum distribution for the target nucleons. In the NOMAD event generator we used the Benhar–Fantoni parametrization [68] (Fig. 7).

The QEL simulation is based on the Smith–Moniz approach [31]. The momentum of the recoil nucleus and the nucleon binding energy are included in the conservation laws which determine the event kinematics. The only final state interaction (FSI) effect which is taken into account at this stage is the Pauli exclusion principle.

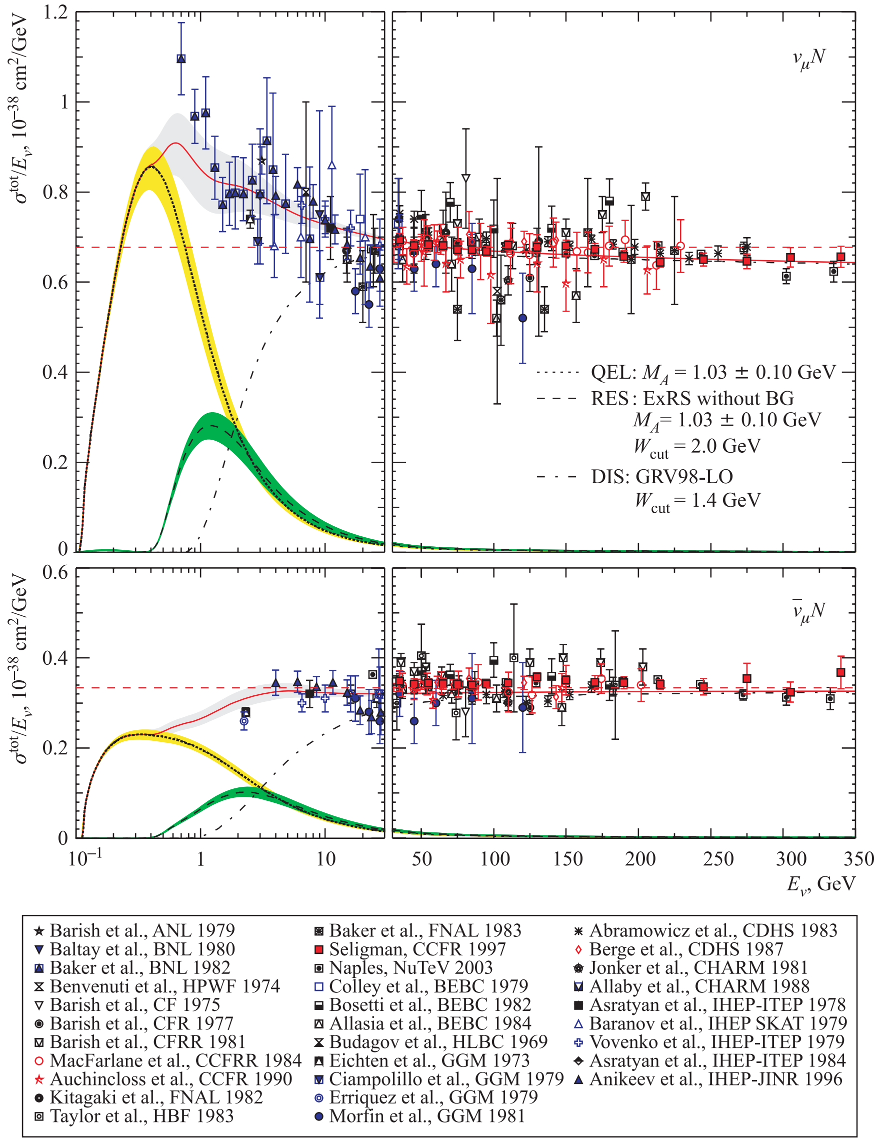

Fig. 6. Slopes of the total ν_μ and $\overline{\nu}_\mu$ CC scattering cross sections off an isoscalar nucleon (experimental data are taken from [54]). The curves and bands show the QEL, RES, and DIS contributions and their sums calculated with the parameters described in the legend of the top panel. The averaged values over all energies $(0.677 \pm 0.014) \cdot 10^{-38}$ cm^2/GeV (for $\nu_\mu N$) and $(0.334 \pm 0.008) \cdot 10^{-38}$ cm^2/GeV (for $\overline{\nu}_\mu N$) obtained by the Particle Data Group [47] are also shown for comparison (straight lines)

MC implementation of the Fermi gas model in the case of single-pion production is more straightforward. First, we generate the momentum of the target nucleon and make a Lorentz boost to its rest frame where the RES event can be simulated according to the extended RS model described in Subsec. 4.2. The effect of Pauli blocking on the outgoing nucleon is taken into account as it is in the QEL MC.

In the case of the DIS neutrino scattering there are several specific nuclear effects (such as nuclear shadowing, pion excess and off-shell corrections to bound nucleon structure functions). They are described in the theoretical framework proposed in [69].

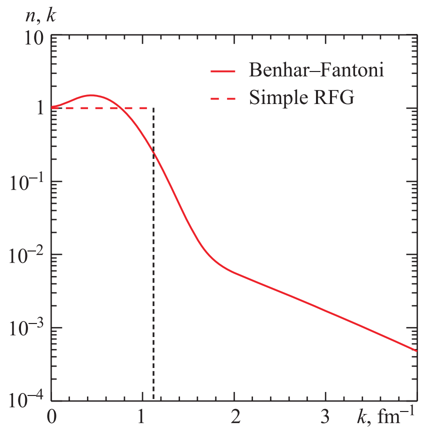

Fig. 7. The Benhar–Fantoni parametrization [68] for the momentum distribution of the target nucleons (solid line), normalized to the Fermi distribution with zero temperature and Fermi momentum $k_F = 221$ MeV (simple RFG, dashed line)

Simulating the re-interactions between particles produced at the primary neutrino collision off the target nucleon with the residual nucleus is an important ingredient of the MC event generator. To include this effect, commonly called final state interactions (FSI), we use the DPMJET package [70].

The intranuclear reinteraction of the particles generated by the QEL, RES or DIS event generators can be described and simulated by the formation zone intranuclear cascade model [71] implemented in DPMJET. Secondaries from the first collision are followed along straight trajectories and may induce in turn intranuclear cascade processes if they reach the end of their «formation zone» inside the target; otherwise they leave the nucleus without interacting.

There are two important parameters in DPMJET. The first one, called the formation time τ_0, controls the development of the intranuclear cascade. With increasing τ_0, the number of cascade generations and the number of low-energy particles will be reduced. Its default value is $\tau_0 = 2.0$.

Inside DPMJET, the momenta of the spectator nucleons are sampled from the zero temperature Fermi distribution. However, the nuclear surface effects and the interaction between nucleons result in a reduction of the Fermi momentum (see Fig. 7). It can be accounted for by introducing a correction factor $\alpha^F_{\rm mod}$ (default value 0.6). Moreover, $\alpha^F_{\rm mod}$ provides the possibility of some modification of the momentum distribution for the emitted low-energy nucleons.

At the end of the intranuclear cascade, the residual nucleus is supposed to go through some deexcitation mechanisms. It can be disrupted into two or more fragments, emit photons, nucleons or light particles (like d, α, ^{3}H, ^{3}He). We can easily neglect this contribution, since the typical energy of those particles is below the registration threshold of the NOMAD detector.

In our analysis, special attention will be devoted to the dependence of the obtained results on the intranuclear cascade parameters. As a cross check, we compare our MC simulation for the QEL process with the predictions of the NUANCE event generator [72], which is currently used in a large number of neutrino experiments.

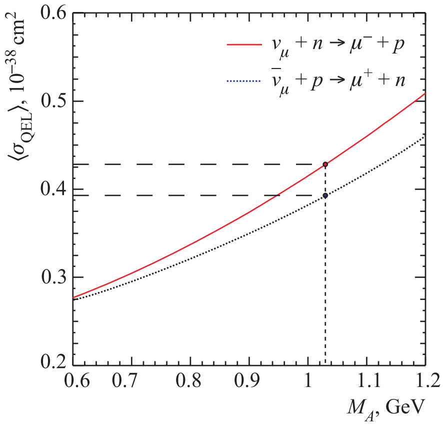

Fig. 8. Flux averaged cross section of QEL (anti)neutrino scattering for NOMAD $\nu_\mu(\bar{\nu}_\mu)$ beam as a function of the axial mass M_A

4.6. Expected Signal/Background Ratio in $\nu_\mu(\bar{\nu}_\mu)$ CC Sample. In this Section we estimate the number of signal quasi-elastic events in the initial $\nu_\mu(\bar{\nu}_\mu)$ CC sample.

Table 3. Flux averaged cross sections of the QEL, RES, DIS CC and NC processes per one nucleon of the NOMAD target. Neutrino beam spectrum corresponds to the $|X, Y| \leqslant 100$ cm fiducial area. The unit used for the cross section is 10^{-38} cm^2

Process type	ν_μ	$\bar{\nu}_\mu$
QEL	0.428	0.393
RES	0.576	0.432
DIS CC	16.643	4.876
DIS NC	5.335	

The contribution of each process to the total set of events is proportional to its flux averaged cross section:

$$\langle\sigma\rangle = \int \sigma(E_\nu)\Phi(E_\nu)dE_\nu \Big/ \int \Phi(E_\nu)dE_\nu, \tag{4}$$

where

$$\sigma(E_\nu) = n_n\sigma_{\nu n}(E_\nu) + n_p\sigma_{\nu p}(E_\nu)$$

is the theoretical prediction for the cross section of the process at stake, $\Phi(E_\nu)$ denotes the NOMAD (anti)neutrino energy spectrum*; $n_n(n_p)$ is the relative fraction of neutrons(protons) in the NOMAD target (see Sec. 3).

The QEL cross section was calculated in the framework of the Smith and Moniz model [31] for carbon with binding energy $E_b = 25.6$ MeV and Fermi momentum $P_F = 221$ MeV. As noted above, the final result depends strongly on the axial mass M_A (see Fig. 8).

To estimate the RES contribution, we fold the extended RS model [51] for a free nucleon with the Pauli factor from [73]. The computation of $\sigma_{\rm dis}(E_\nu)$ has been done with the GRV98-LO PDF model as indicated in [54]. The cutoff parameters $W_{\rm cut}^{\rm RES}$ and $W_{\rm cut}^{\rm DIS}$ are the same as for the MC simulation.

Table 3 contains our results for the reduced fiducial volume of the NOMAD detector: $|X, Y| \leqslant 100$ cm; the average ν_μ ($\bar{\nu}_\mu$) energy was 25.9 (17.6) GeV.

Combining all these, the expected fraction of quasi-elastic events in the initial $\nu_\mu(\bar{\nu}_\mu)$ CC sample before any special selection is about 2.4% (6.9%) or ~ 20300 (~ 1360) events.

5. EVENTS SELECTION

In this Section we describe particular features of reconstruction and identification of QEL events.

For a $\nu_\mu n \to \mu^- p$ event one can expect two tracks originating from the reconstructed primary vertex**: one of them should be identified as a muon, while the second track is assumed to be a proton. Later we shall refer to events with such a topology as 2-track (two track) events***.

Sometimes the proton track cannot be reconstructed if its momentum is below the detector registration threshold. In this case, we deal with only one muon track and we call such an event a 1-track (single track) event.

There are three possible reasons for the reconstruction of the proton track in a QEL event to fail:

• The proton, which was born in the neutrino interaction with the target nucleon, has too low momentum or too large emission angle (this depends on

---

*The procedure used for the calculation of the flux and composition of the CERN SPS neutrino beam is described in [30].

**All charged tracks originating within a 5 cm box around the reconstructed primary vertex are forced to be included into it; we have also tried to vary this parameter by enlarging the size of the box to 10 cm and found that the final results are rather stable (within 0.3% for the measured QEL cross section).

***In this analysis we do not take into account clusters in the electromagnetic calorimeter, which can be associated with neutral particles, originating from the primary vertex.

the parameters of the model used to describe the neutrino–nucleon interaction, in particular, on the value of the axial mass).

• The proton from the primary neutrino interaction was involved in an intranuclear cascade and lost part of its energy (this is controlled by the DPMJET parameters, mainly by the formation time τ_0).

• The detector magnetic field deviates positively charged particles upwards; therefore, if a slow proton is emitted at an azimuth $\varphi_h \sim \pi/2$, its trajectory is almost parallel to the drift chamber planes and its track reconstruction efficiency (which depends on the number of hits associated with the track) is significantly lower than in the case of a proton emitted downwards at $\varphi_h \sim 3\pi/2$.

In Fig. 9 we illustrate these last two effects: the magnetic field is the cause of the asymmetry in the azimutal distribution of the reconstructed protons, while variyng the formation time parameter τ_0 affects the expected number of tracks uniformly.

In Fig. 10 we display an example of distributions of the leading proton momentum p_h and emission angle θ_h before and after FSI for the QEL neutrino scattering. The proton reconstruction probabilities are also shown as functions of p_h and θ_h: one can observe a fast decrease at low proton momenta (below 300 MeV/c) and large emission angles (larger than 72°). So, FSI tends to increase the fraction of events in kinematic domains with low proton reconstruction efficiency and therefore to change the expected fraction of events with a given topology in the identified QEL sample.

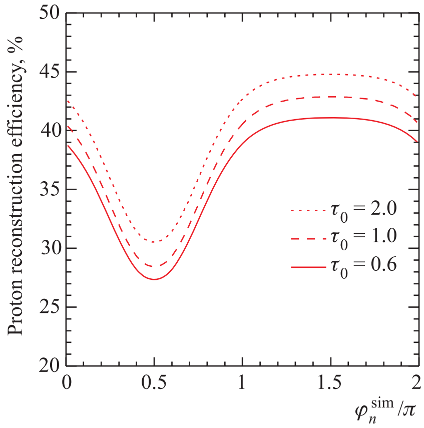

Fig. 9. The reconstruction efficiency of proton track as a function of its azimuth φ_h for ν_μ QEL scattering. The curves are smoothed MC predictions obtained for different values of the formation time τ_0

Using 2-track events only for the analysis may seem very attractive, since we could significantly reduce the background contamination with the help of additional kinematic variables (details can be found below). However, the results thus obtained might still have large systematic uncertainties coming from insufficient understanding of nuclear effects.

The QEL events which are not reconstructed as 2-track events will populate mainly the 1-track sample. But $\sigma_{\rm qel}$ extracted from this sample will suffer from the

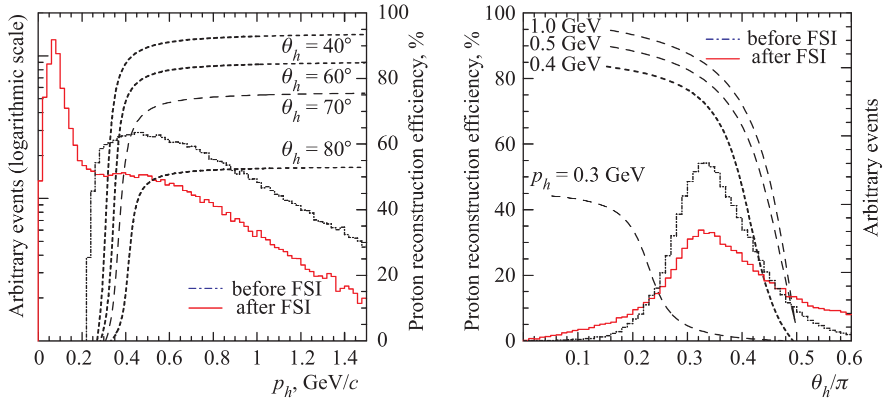

Fig. 10. Distribution of the leading proton momentum (left) and emission angle (right) before (dash-dotted line) and after (solid line) FSI simulation. Dashed lines show the proton reconstruction efficiency as function of the proton momentum and emission angle (for $\pi < \varphi_h < 2\pi$)

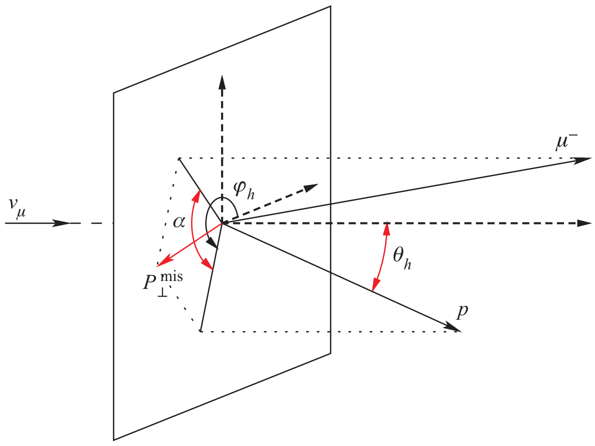

Fig. 11. Likelihood variables: missing transverse momentum $P_\perp^{\rm mis}$, proton emission angle θ_h, angle α between the transverse components of the charged tracks

same source of uncertainty. However, the measurement of the QEL cross section simultaneously from both samples is expected to have only little dependence on the uncertainties in the modeling of FSI effects and this is indeed what is found in the data (see Sec. 8).

Therefore, the strategy of our analysis (selection criteria) in the case of $\nu_\mu n \to \mu^- p$ can be outlined as follows:

• *Fiducial volume cut.* The reconstructed primary vertex should be within the restricted* fiducial volume (FV):

$$|X, Y| \leqslant 100 \text{ cm}, \quad 25 \leqslant Z \leqslant 395 \text{ cm}. \tag{5}$$

• *Identified muon.* We require the presence of a reconstructed and identified negatively charged muon. In order to avoid possible problems with detector reconstruction inefficiencies, we require $0 < \varphi_\mu < \pi$, where φ_μ is the muon azimuthal angle (so, the proton track should lie in the bottom hemisphere).

• *Event topology and reconstructed kinematic variables.* We assign the events to the 1-track and 2-track subsamples and calculate E_ν and Q^2.

• *Single track sample* (only one charged lepton is reconstructed and identified). To avoid contamination from the through-going muons we extrapolate the muon track to the first drift chamber and require the absence of veto chamber hits in the vicinity of the intersection point. The efficiency of this quality cut was controlled by visual scanning of the reconstructed 1-track events in the experimental data and was found to be satisfactory. Another quality cut was used to suppress a possible contribution from inverse muon decay events: we require the muon transverse momentum to be greater than 0.2 GeV (see Subsec. 6.1.1 for more details).

The kinematic variables are reconstructed under the assumption that the target nucleon is at rest. For the 1-track events, the muon momentum is the sole measurement and we have to use the conservation laws (assuming QEL) to compute other kinematic quantities:

$$\begin{aligned}
&E_\nu = \frac{ME_\mu - m_\mu^2/2}{M - E_\mu + p_\mu \cos\theta_\mu}, \\
&Q^2 = 2M(E_\nu - E_\mu), \\
&p_h = ((E_\nu - p_\mu \cos\theta_\mu)^2 + p_\mu^2 \sin^2\theta_\mu)^{1/2}, \\
&\cos\theta_h = (E_\nu - p_\mu \cos\theta_\mu)/p_h,
\end{aligned} \tag{6}$$

where p_μ, θ_μ (p_h, θ_h) are the momentum and emission angle of the outgoing muon (nucleon). With the help of the MC simulation we estimate the resolution of the reconstructed E_ν and Q^2 as 3.6 and 7.8%, respectively.

• *Two track sample* (both the negative muon and the positively charged track are reconstructed). For a reliable reconstruction, we require that the number of

*We use a more stringent cut $Z > 50$ cm for the data collected during 97 and 98, when the first drift chamber module was substituted by the NOMAD STAR detector.

hits associated with the positively charged track should be greater than 7 and its momentum $p_h > 300$ MeV/c. Otherwise such an event is downgraded to the 1-track sample. For 2-track events, we use both the muon and the proton reconstructed momenta to estimate E_ν and Q^2:

$$\begin{aligned} E_\nu &= p_\mu \cos\theta_\mu + p_h \cos\theta_h, \\ Q^2 &= 2E_\nu(E_\mu - p_\mu \cos\theta_\mu) - m_\mu^2. \end{aligned} \tag{7}$$

The expected resolutions for E_ν and Q^2 are 3.6 and 7.1%.

• *Background suppression.* The contamination from RES and DIS processes can be suppressed by using the difference between kinematical distributions in the QEL and background events as well as by the identification of the reconstructed positively charged track as a proton (for the 2-track sample). Therefore we apply:

Identification of the positively charged track

Momentum-range method [74] can be reliably applied for low energy protons since their tracks are shorter compared to that of π^+ (the main background for proton identification) due to larger ionization losses. In our case, this method can be applied to about 17% of the events.*

Kinematical criteria

In the case of the 2-track sample, we can use additional kinematic variables to suppress background contamination. We build the likelihood ratio

$$\mathcal{L} = \ln \frac{\mathcal{P}(\vec{\ell}\,|\mathrm{QEL})}{\mathcal{P}(\vec{\ell}\,|\mathrm{BG})}, \tag{8}$$

using 3-dimensional correlations between the following variables (see Fig. 11):

1) missing transverse momentum: $P_\perp^{\mathrm{mis}} < 0.8$ GeV/c;
2) proton emission angle: $0.2 \leqslant \theta_h/\pi \leqslant 0.5$;
3) angle α between the transverse components of the charged primary tracks: $\alpha/\pi \geqslant 0.8$.

Here $P(\vec{\ell}\,|\mathrm{QEL})$ and $P(\vec{\ell}\,|\mathrm{BG})$ are the probabilities for signal and background events to have the values of the kinematic variables $\vec{\ell} = (P_\perp^{\mathrm{mis}}, \theta_h, \alpha)$. We have

---

*We also undertook an attempt to identify positively charged particles using the TRD information. A special algorithm [75, 76] can be potentially used for discrimination between two particle ID hypotheses (p/π in our case). However, a low momentum (~ 0.9 GeV) of the particle and a rather large emission angle ($\gtrsim 45°$) result in that either the particle does not reach the TRD or the number of residual TRD hits is not large enough for the identification. Therefore, the TRD algorithm could be applied only to a limited fraction of events ($\sim 6\%$) and cannot play any significant role in our analysis.

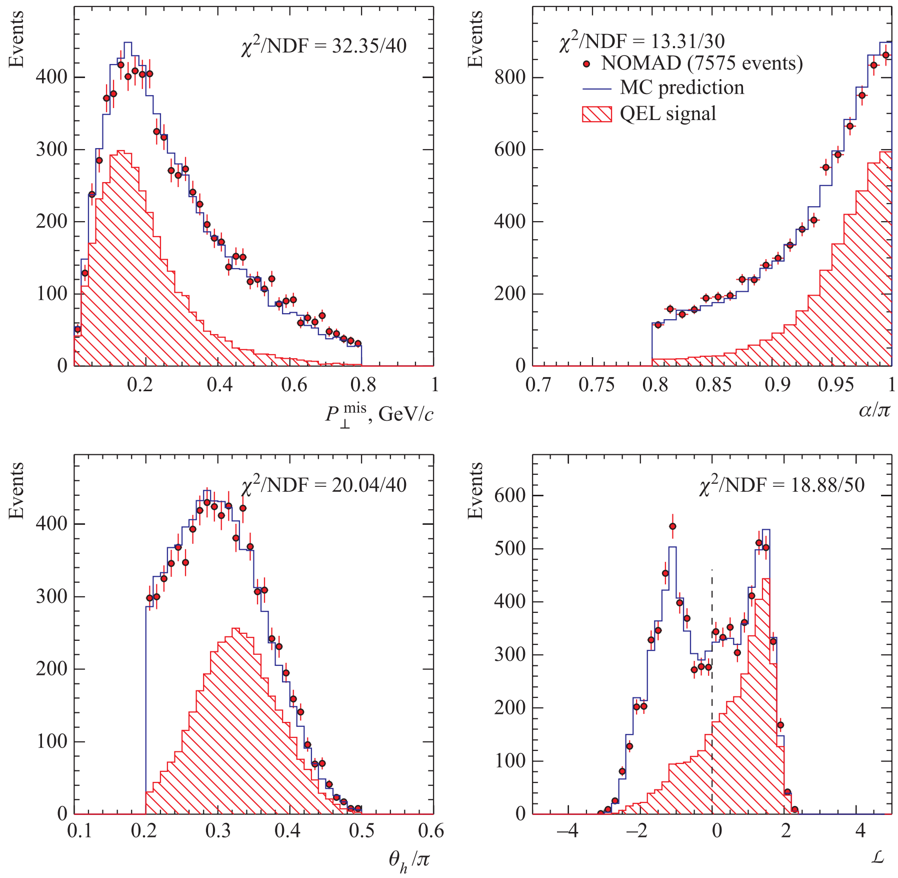

Fig. 12. The $P_\perp^{\rm mis}$, α, θ_h and likelihood distributions for a mixture of QEL, RES and DIS simulated events compared to real data

found that the DIS and RES probability functions are very similar; therefore we build the likelihood function taking only resonance events for the denominator of Eq. (8).

The comparison of $P_\perp^{\rm mis}$, α, θ_h and $\mathcal{L}$ distributions in the data with the proper mixture of simulated QEL, RES and DIS events is displayed in Fig. 12. The good agreement observed between MC predictions and experimental data confirms a reasonable understanding of the background contaminations and reconstruction efficiency in our analysis.

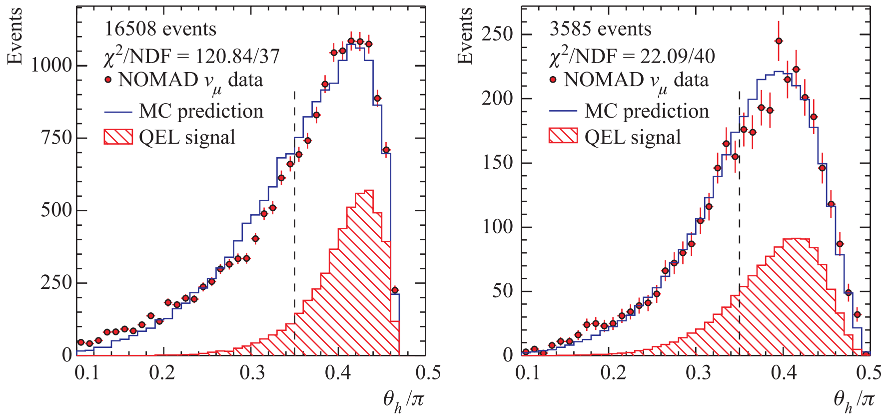

Fig. 13. The θ_h distributions for single track ν_μ and $\bar{\nu}_\mu$ samples

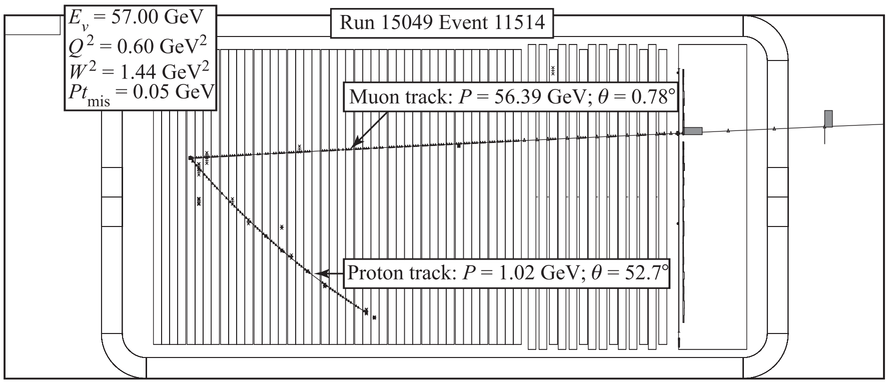

Fig. 14. A typical example of data event (run 15049 event 11514) identified as $\nu_\mu n \to \mu^- p$ in this analysis. Long track is identified as muon, short track is assumed to be proton

In the case of 1-track events, our abilities to suppress background contamination are limited since all kinematic variables are expressed in terms of the muon momentum p_μ and emission angle θ_μ with the help of the conservation laws for QEL events. Therefore, the proton reconstructed emission angle, Eq. (6), can be considered as an analog of the likelihood function (see Fig. 13).

The explicit values for the kinematic selection criteria ($\mathcal{L} \geqslant 0$ for the 2-track sample and $0.35 \leqslant \theta_h/\pi \leqslant 0.5$ for the 1-track sample) were found from the optimization of the sensitivity $\mathrm{SG}/\sqrt{\mathrm{SG}+\mathrm{BG}}$, where SG and BG are

Table 4. Number of events $N_{\rm data}$ in ν_μ and $\bar{\nu}_\mu$ QEL samples; expected selection efficiency, purity and background contaminations (BG)

	ν_μ sample			$\bar{\nu}_\mu$ sample
	Single track	Two tracks	Total	Single track
$N_{\rm data}$	10358	3663	14021	2237
Efficiency (%)	21.3	13.3	34.6	64.4
QEL purity (%)	41.7	73.9	50.0	36.6
DIS BG (%)	34.5	15.9	29.7	33.5
RES BG (%)	23.2	10.2	19.8	28.5
Other BG (%)	< 0.6	< 0.1	< 0.5	1.3

the expected numbers of signal and background events in the identified QEL sample.

The investigation of antineutrino sample is a much simpler task since these events are mostly ($\sim 96\%$ of cases) reconstructed as 1-track events (we have no hits from outgoing neutrons in the drift chambers). Therefore, we require identification of the positively charged muon and follow the procedure for the 1-track sample discussed above. The only difference is the absence of contamination from the inverse muon decay events, so we do not need to apply the quality cut on the transverse muon momentum.

In Table 4 we summarize the information about the selection of samples with $\nu_\mu n \to \mu^- p$ and $\bar{\nu}_\mu p \to \mu^+ n$ candidates in the data. An example of the 2-track event from real data identified as $\nu_\mu n \to \mu^- p$ is displayed in Fig. 14.

6. THE QEL CROSS-SECTION AND AXIAL MASS MEASUREMENT

In this Section we describe our analysis procedure. The QEL cross-section measurement using normalization either to the DIS events or to the IMD events is first presented in Subsec. 6.1, afterwards, we describe the procedure used to extract the value of the axial mass M_A from the fit of the Q^2 distribution. This is the subject of Subsec. 6.2.

6.1. The QEL Cross-Section Measurement. Since there was no precise knowledge of the integrated neutrino flux in the NOMAD experiment, we use a different process with a better known cross section, recorded at the same time, for the normalization of the QEL cross section. A similar procedure was often applied in the previous neutrino experiments as, for example, CERN BEBC [18]. Moreover, the use of another process recorded in the same experimental runs allows one to reduce significantly the systematic uncertainty related to the detector material composition. Nevertheless, this auxilliary process must meet two requirements: its cross section should be measured with rather high accuracy and the corresponding events can easily be extracted from the full data sample.

Let us divide the investigated interval of neutrino energy into several bins and enumerate them with index $i = 1..N_E$. Then, the number of identified QEL events in the ith bin with boundaries $[E_i, E_{i+1}]$ is

$$N_i^{\rm data} = N_i^{bg} + C \sum_{j=1}^{N_E} \varepsilon_{ij}^{\rm qel} \Phi_j \langle \sigma_{\rm qel} \rangle_j, \qquad (9)$$

where

$$\Phi_i = \int_{E_i}^{E_{i+1}} \Phi(E)\, dE, \quad \sum_{i=1}^{N_E} \Phi_i = 1$$

and

$$\langle \sigma_{\rm qel} \rangle_i = \frac{1}{\Phi_i} \int_{E_i}^{E_{i+1}} \sigma_{\rm qel}(E) \Phi(E)\, dE.$$

Coefficient C accumulates the absolute neutrino flux and the number of target nucleons. The matrix element $\varepsilon_{ij}^{\rm qel}$ is the probability that the reconstructed neutrino energy E_ν of a QEL event falls into the ith bin, while the simulated energy actually belongs to the jth bin.

The expected background contamination is

$$N_i^{bg} = C \left(\varepsilon_i^{\rm res} \langle \sigma_{\rm res} \rangle + \varepsilon_i^{\rm dis} \langle \sigma_{\rm dis} \rangle \right), \qquad (10)$$

where we use the definition of Eq. (4) for $\langle \sigma_{bg} \rangle$; ε_i^{bg} denotes the renormalized energy distribution in BG events passing the QEL identification procedure:

$$\sum_{i=1}^{N_E} \varepsilon_i^{bg} = \varepsilon^{bg} = N_{\rm rec}^{bg} / N_{\rm sim}^{bg}, \qquad (11)$$

here $N_{\rm sim}^{bg}$ and $N_{\rm rec}^{bg}$ are the numbers of MC events simulated and identified as QEL in the chosen detector FV.

Similar equations can be written for any other process recorded in the same detector FV. If we identify N_0 events of a process, whose flux averaged cross section in an energy interval containing these events is σ_0, we can write

$$N_0 = C\, \Phi_0 \sigma_0,$$

where Φ_0 is the relative part of the neutrino flux belonging to the same energy interval (we assume that N_0 is background subtracted and efficiency corrected).

We can now get rid of C and write the final equation for $\langle \sigma_{\rm qel} \rangle_i$:

$$\langle \sigma_{\rm qel} \rangle_i = \frac{1}{\Phi_i} \sum_{j=1}^{N_E} (\varepsilon_{\rm qel}^{-1})_{ij} \left[N_j^{\rm data} \frac{\Phi_0 \sigma_0}{N_0} - \varepsilon_j^{\rm res} \langle \sigma_{\rm res} \rangle - \varepsilon_j^{\rm dis} \langle \sigma_{\rm dis} \rangle \right]. \qquad (12)$$

Numerical values for $\langle\sigma_{\rm res}\rangle$ and $\langle\sigma_{\rm dis}\rangle$ are given in Table 3. The efficiencies $\varepsilon_{ij}^{\rm qel}$, $\varepsilon_i^{\rm res}$ and $\varepsilon_i^{\rm dis}$ should be estimated with the help of the MC simulation for QEL, RES and DIS samples separately; the factor $\Phi_0\sigma_0/N_0$ comes from the auxilliary process used for normalization.

Let us note that the smearing of the reconstructed neutrino energy is taken into account in Eq. (12) by the inverse matrix of QEL efficiencies.

Equation (12) can also be applied to the entire energy interval. In this case, we can use the usual notations for efficiencies as in Eq. (11). From the measured $\langle\sigma_{\rm qel}\rangle$ we calculate the axial mass M_A by using the Smith and Moniz formalism (see Fig. 8).

In the following Subsections, we investigate the DIS and IMD processes which can both be used for the QEL cross-section normalization as just described.

Possible sources of systematic errors in our analysis procedure are discussed in Sec. 7.

6.1.1. Dis Events Selection. The phenomenology of neutrino DIS is well developed. Experimental data are in rather good agreement with theoretical predictions. The charged current neutrino DIS is an inclusive process and for its selection from the data sample, the following criteria are enough:

• *Fiducial volume cut.* The primary vertex should be in the same FV as that defined for the QEL events, see Eq. (5).

• *Muon identification and topology cut.* At least two charged tracks should originate from the primary vertex; one of them should be identified as a muon (μ^- in the case of ν_μ CC and μ^+ for $\bar{\nu}_\mu$ CC).

• *Background suppression.* The third criterium is used to avoid contributions from the QEL and RES events. We have checked three different possibilities for it:

1) The total visible energy in the event should be $E_\nu \leqslant 300$ GeV and the reconstructed hadronic mass $W \geqslant 1.4$ GeV; in this case the computation of $\langle\sigma_{\rm dis}\rangle$ has been done for GRV98-LO PDF model according to the prescriptions in [54].

2) We keep the requirement for the reconstructed hadronic mass ($W \geqslant 1.4$ GeV) but reduce the neutrino energy region to $40 \leqslant E_\nu \leqslant 200$ GeV; theoretical calculation of $\langle\sigma_{\rm dis}\rangle$ is also done with the help of [54].

3) Using the same neutrino energy interval as in the item 2 ($40 \leqslant E_\nu \leqslant 200$ GeV), we remove the cut on the reconstructed hadronic mass W. In this

Table 5. Selection of the DIS events in ν_μ and $\bar{\nu}_\mu$ CC samples. Total efficiency (in %), expected purity of selected events (in %), theoretical prediction for $\langle\sigma_{\rm dis}\rangle$, observed $N_{\rm data}$ and corrected N_0 number of events in experimental data are given for each variant of DIS selection described above

Variant of selection	ν_μ sample			$\bar{\nu}_\mu$ sample		
	1	2	3	1	2	3
Efficiency	82.95	86.84	88.52	75.46	81.40	83.20
Purity	97.10	98.62	99.62	71.48	72.57	73.95
$N_{\rm data}$, events	676702.0	267517.0	276018.0	17744.0	7996.0	8500.0
N_0, events	792162.0	303790.7	310617.3	16807.1	7128.6	7553.4
Relative flux Φ_0	1	0.144	0.144	1	0.106	0.106
$\langle\sigma_0\rangle$, 10^{-38} cm^2	16.643	44.876	46.069	4.876	20.124	21.999
C^{-1}, 10^{-43} cm^2	2.101	2.127	2.136	29.012	29.924	30.872

case, we take the total CC neutrino–nucleon cross section to be*:

$$\sigma_\nu^{\rm tot}(E_\nu)/E_\nu = (0.677 \pm 0.014) \cdot 10^{-38}\ {\rm cm}^2/{\rm GeV},$$
$$\sigma_{\bar{\nu}}^{\rm tot}(E_\nu)/E_\nu = (0.334 \pm 0.008) \cdot 10^{-38}\ {\rm cm}^2/{\rm GeV}$$

(PDG average [47]). The calculated $\langle\sigma_{\rm tot}\rangle$ should be corrected due to the fact that NOMAD target is slightly nonisoscalar.

The numerical results of the DIS events selection can be found in Table 5. For the QEL cross-section normalization we use results obtained with the last method (PDG based) as having the most solid ground. Thus, the final normalization is performed to the total ν_μ ($\bar{\nu}_\mu$) CC cross section. We also checked that this normalization is consistent with two previous calculations based on approach from [54] within 1.6% (5.9%) for ν_μ ($\bar{\nu}_\mu$) CC sample.

6.1.2. Inverse Muon Decay Events Selection. Inverse muon decay (IMD) $\nu_\mu e^- \to \mu^- \nu_e$ is a purely leptonic process, which is well known both on theoretical and experimental grounds. Its cross section in the Born approximation is

$$\sigma_{imd}(E_\nu) = \sigma_{as} E_\nu \left(1 - \frac{m_\mu^2}{2 m_e E_\nu}\right)^2. \qquad (13)$$

The numerical value of the constant σ_{as} calculated in the framework of the Standard Model was found to be in good agreement with experimental measurements [78]:

$$\sigma_{as} = \frac{2 m_e G_F^2}{\pi} = 1.723 \cdot 10^{-41}\ {\rm cm}^2\ {\rm GeV}^{-1}. \qquad (14)$$

*The CHORUS measurement for the CH_2 target [77] is consistent with this value.

The number of IMD events N_0 is proportional to its flux averaged cross section from Eq. (4):

$$\langle \sigma_{imd} \rangle = 1.017 \cdot 10^{-40}\ \text{cm}^2 \tag{15}$$

and expected to be at least 650 times smaller than the number of DIS events.

To select the IMD events we require:

• The primary vertex should be in the same fiducial volume as that used with identified QEL events, see Eq. (5).

• There is only one negatively charged track originating from the primary vertex; it should be identified as a muon.

• There are no veto chamber hits in the vicinity of the intersection point of the extrapolated muon track and the first drift chamber (quality cut, the same as for 1-track events from the QEL sample).

• The muon energy is above the threshold:

$$E_\mu \geqslant \frac{m_\mu^2 + m_e^2}{2m_e} = 10.93\ \text{GeV}. \tag{16}$$

• The transverse momentum $p_\perp$ of the muon produced in IMD event is very limited by kinematics: $p_\perp^2 \leqslant 2m_e E_\mu$.

In this sample the contamination from the reaction $\bar{\nu}_e e \to \mu^- \bar{\nu}_\mu$ is estimated to be at the level of $\sim 10^{-3}$, e.g. well below 1 event, since the ratio of the fluxes $\bar{\nu}_e/\nu_\mu$ is 0.0027 [30] while the ratio of the cross sections is $\sigma(\bar{\nu}_e e \to \mu^- \bar{\nu}_\mu)/\sigma(\nu_\mu e \to \mu^- \nu_e) \approx 1/3$.

We determine the number of signal events N_{imd} from the fit of the $p_\perp^2$ distribution to experimental data with the function $F(p_\perp^2)$:

$$F(p_\perp^2) = N_{imd} F_{imd}(p_\perp^2) + [N_{\text{data}} - N_{imd}]\, F_{bg}(p_\perp^2), \tag{17}$$

where F_{imd} and F_{bg} are the normalized MC expectations for signal and background $p_\perp^2$ distributions; N_{data} denotes the number of events in real data which passed all selection criteria.

The QEL events are now playing the role of the most important background for the IMD selection. However, the contaminations from the RES and DIS events cannot be neglected since they distort the shape of the $p_\perp^2$ distribution. As usual, the relative contribution of each process to the expected background is proportional to the corresponding efficiency and flux averaged cross section (see Table 3).

Expression (17) contains only one free parameter N_{imd}, which is the number of observed IMD events. Finally, we find $N_{imd} = 436.0 \pm 28.5$ with the quality of the fit $\chi^2/\mathrm{NDF} = 0.89$ (see Fig. 15). Taking into account that the selection efficiency for the IMD events is 87.8% we report the total number of IMD events N_0, which can be used for the QEL normalization:

$$N_0 = 496.6 \pm 32.5. \tag{18}$$

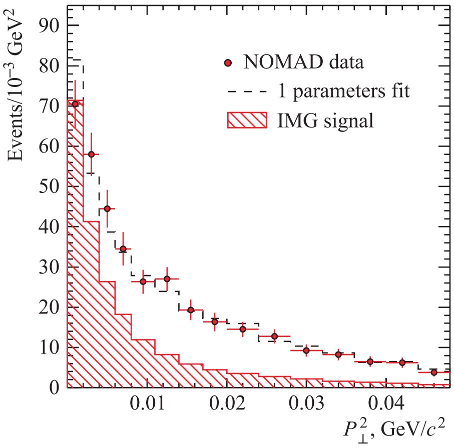

Fig. 15. Inverse muon decay: NOMAD experimental data, $p_\perp^2$ distribution

The relative error for σ_0/N_0 in the IMD case is about 7% (due to the small size of the IMD sample). Nevertheless the factor itself is in agreement (within $\sim 4\%$) with the evaluation based on the DIS sample (see Table 5).

We emphasize here that the use of the IMD process for the normalization is an important independent cross check for the measurement of the QEL cross section. Especially it allows one to verify that there are no experimental effects related to potential trigger inefficiency for selection of low multiplicity neutrino interactions (single muon going through the trigger planes).

6.2. Axial Mass Measurement from the Q^2 Distribution. To extract the axial mass from the Q^2 distribution the experimental data are fitted to the theoretical predictions using a standard χ^2 method. We bin the events in two variables Q^2 and E_ν (in the case of a single E_ν interval our procedure can be considered as the usual 1-dimensional fit)*.

Let us enumerate bins with index $i = 1..N_B$; bin $i = N_B + 1$ contains events which fall outside of the investigated (E_ν, Q^2) region. It is convenient to define boundaries in such a way that each bin with $i = 1..N_B$ contains approximately the same number of experimental events passing all identification criteria.

A minimization functional is

$$\chi^2(M_A) = \sum_{i=1}^{N_B} \frac{\left[N_i^{\mathrm{data}} - N_i^{\mathrm{th}}(M_A)\right]^2}{N_i^{\mathrm{data}}}, \tag{19}$$

*In practice it is convenient to use dimensionless variables (a, b) instead of (E_ν, Q^2). Then, $E_\nu = E_\nu^{\min} + a(E_\nu^{\max} - E_\nu^{\min})$ and $Q^2 = Q^2_{\min}(E_\nu) + b[Q^2_{\max}(E_\nu) - Q^2_{\min}(E_\nu)]$. So, $a, b \in [0, 1]$.

where $N_i^{\rm data}$ is the number of events in the ith bin of the nonweighted experimental distribution, while $N_i^{\rm th}$ is a superposition of the normalized MC background N_i^{bg} and the expected QEL signal:

$$N_i^{\rm th}(M_A) = N_i^{bg} + C \sum_{j=1}^{N_B+1} \varepsilon_{ij}^{\rm qel} \Phi_j \langle\tilde{\sigma}_{\rm qel}\rangle_j. \tag{20}$$

This equation is similar to Eq. (9), N_i^{bg} being defined in the same way as in Eq. (10); $\varepsilon_{ij}^{\rm qel}$ is the probability that a QEL event simulated in the jth bin is reconstructed in the ith bin. The QEL scattering dynamics is described by the following term:

$$\langle\tilde{\sigma}_{\rm qel}\rangle_i = \frac{1}{\Phi_i} \int_{\Omega_i} \frac{d\sigma}{dQ^2}(E, Q^2, M_A)\Phi(E)\, dE dQ^2, \tag{21}$$

$$\Phi_i \langle\tilde{\sigma}_{\rm qel}\rangle_i \,|_{i=N_B+1} = \langle\sigma_{\rm qel}\rangle - \sum_{j=1}^{N_B} \Phi_j \langle\tilde{\sigma}_{\rm qel}\rangle_j, \tag{22}$$

here Ω_i denotes the (E_ν, Q^2) interval, which corresponds to the ith bin; $d\sigma/dQ^2$ is the differential QEL cross section on bound target nucleons.

The coefficient C can be defined in either of two ways:

1) The $N_i^{\rm th}$ distribution is normalized to the total number of events in the experimental data:

$$\sum_{i=1}^{N_B} N_i^{\rm th} = \sum_{i=1}^{N_B} N_i^{\rm data}. \tag{23}$$

In this case, the proposed method should be sensitive only to the shape of the distribution but not to the absolute number of identified events (contrary to the M_A measurement from the total QEL cross section).

2) C is defined in the same way as for the total QEL cross-section measurement, i.e., we use another process (DIS) for normalization:

$$C = \frac{N_0}{\Phi_0 \sigma_0}. \tag{24}$$

If we sum over the Q^2 variable for the investigated (E_ν, Q^2) interval, finding the M_A parameter from Eq. (19) becomes nothing else than the numerical resolution of Eq. (9). Therefore, this variant of the fit can be considered as a simultaneous fit of the total and differential cross sections; henceforth, we shall refer to it as $\sigma \otimes d\sigma/dQ^2$ fit.

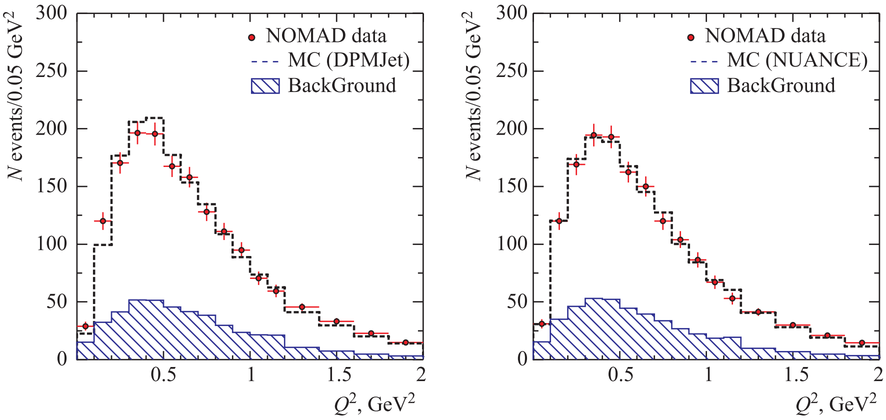

Fig. 16. The Q^2 distributions in identified QEL events in comparison with different MC predictions DPMJET (left) and NUANCE (right)

Figure 16 presents a comparison of the reconstructed Q^2 distribution with different MC predictions (DPMJET with $\tau_0 = 1$, $\alpha^F_{\rm mod} = 0.6$ and NUANCE). The expected background contamination is also shown.

We can now apply the proposed methods to experimental data and measure the QEL cross section and axial mass M_A. The numerical results are reported in Sec. 8, while the discussion of the corresponding uncertainties is presented in the next Section.

7. SYSTEMATIC UNCERTAINTIES

We have studied several sources of systematic uncertainties, which are important for the measurement of the total QEL cross section and axial mass parameter. They are listed below:

1) Identification of QEL events; we vary the selection criteria within reasonable limits ($\mathcal{L} > 0 \pm 0.4$ for 2-track sample and $\theta_h/\pi > 0.35 \pm 0.03$ for 1-track sample).

2) Uncertainty in the total (mainly DIS) charged current muon neutrino cross section, which enters both in the normalization factor σ_0/N_0 and in the subtraction of the corresponding DIS background (the experimental error on $\langle\sigma\rangle_{\rm dis}$ is 2.1% for ν_μ CC and 2.4% for $\bar{\nu}_\mu$ CC).

3) Uncertainty in the RES cross section, which determines the contamination admixture of the single resonant pion events in the identified QEL sample (we assume 10% error on $\langle\sigma\rangle_{\rm res}$ both for neutrino and antineutrino cases).

4) FSI interactions (we vary τ_0 and $\alpha^F_{\rm mod}$ DPMJET parameters for fixed $M_A^{mc} = 1.03$ GeV).

5) Uncertainty in the neutrino flux shape (the relative errors for each E_ν bin were taken from [30]).

6) Neutral current admixture (we assume 5% error for the corresponding cross section, which can be found in Table 3).

7) Charge misidentification of the primary lepton (reconstructed ν_μ CC event is classified as $\bar{\nu}_\mu$ CC and vice versa).

8) Contamination from coherent pion production (see Subsec. 4.4).

In Table 6 we present our numerical estimations for systematic uncertainties (in the case of ν_μ scattering, systematic errors were calculated for the mixture of 1-track and 2-track subsamples). One can see that the most important contributions come from the QEL identification procedure and from the uncertainty on the non-QEL processes contribution to the selected sample of signal events.

The nuclear reinteractions (FSI effect) significantly affect the neutrino sample only (see Table 7), while in the antineutrino case the influence of the nuclear reinteractions is expected to be negligible. For ν_μ scattering, the cross sections can be calculated separately for both the 1-track and 2-track subsamples of identified QEL events or for their mixture. We can then compare the results and choose whichever one has the minimal total error. In our case it was obtained for the

Table 6. The systematic uncertainties (in %) of the QEL cross section $\langle\sigma_{\rm qel}\rangle$ and axial mass M_A, measured in $\nu_\mu n \to \mu^- p$ and $\bar{\nu}_\mu p \to \mu^+ n$ reactions

Source	$\langle\sigma\rangle_{\nu_\mu}$	$M_A[\langle\sigma\rangle_{\nu_\mu}]$	$M_A[d\sigma_\nu/dQ^2]$	$\langle\sigma\rangle_{\bar{\nu}_\mu}$	$M_A[\langle\sigma\rangle_{\bar{\nu}_\mu}]$
Identification procedure	3.6	3.3	2.4	4.3	4.2
$\delta(\sigma_{\rm dis})$	2.9	2.6	0.2	4.2	4.2
$\delta(\sigma_{\rm res})$	4.0	3.6	0.6	7.6	7.4
Nuclear reinteractions	2.4	2.1	6.5	–	–
Shape of $\nu(\bar{\nu})$ spectrum	0.2	0.2	0.1	0.9	0.9
NC contribution	< 0.1	< 0.1	–	1.1	1.1
Muon misidentification	< 0.1	< 0.1	–	1.0	1.0
Coherent pion production	< 0.1	< 0.1	< 0.1	1.1	1.1
Total	6.5	5.9	7.0	9.9	9.5

combined 1-track and 2-track samples, which ware found to be almost insensitive to the variation of DPMJET parameters (see Sec. 8 for explanations).

The uncertainty on the shape of the (anti)neutrino spectrum is important for the measurement of $\sigma_{\rm qel}$ as a function of neutrino energy E_ν. But it does not affect both the flux averaged cross section $\langle\sigma_{\rm qel}\rangle$ and the M_A extraction from the Q^2 distribution.

The uncertainty due to the primary lepton misidentification and neutral currents comes into play through the subtraction of the corresponding background from the selected DIS sample, that is, from the normalization factor. The admixture of those events into the identified QEL events is expected to be negligible.

8. RESULTS

8.1. $\nu_\mu n \to \mu^- p$ **Sample.** The results of our analysis for the ν_μ sample are summarized in Table 7. We measure the flux averaged QEL cross section in the neutrino energy interval 3–100 GeV (see Eq. (12)) for the 1-track and 2-track samples as well as for their mixture (which is called «*combined*» in Table 7). For each $\langle\sigma_{\rm qel}\rangle$ we calculate the corresponding axial mass value, M_A. Results on M_A extraction both from the standard Q^2 fit and from the combined $\sigma \otimes d\sigma/dQ^2$ fit are also given. These measurements are repeated for several QEL MC with different values of input parameters (the axial mass M_A was varied between 0.83 and 1.23 GeV in steps of 0.1 GeV; the formation time τ_0 was allowed one to take a value of 0.6, 1.0 and 2.0; the correction factor $\alpha^F_{\rm mod}$ was varied within the interval $[0.54, 0.69]$). On top of this the NUANCE QEL MC with its own FSI effects is used for cross checks.

We then observe that M_A recalculated from the measured $\langle\sigma_{\rm qel}\rangle$ depends on τ_0 if one refers to the 1-track or 2-track samples. Specifically, the measured M_A value increases with increasing τ_0 when extracted from the 1-track sample while it decreases when extracted from the 2-track sample. This can be understood if we take into account the fact that the τ_0 parameter controls the probability for an outgoing nucleon to be involved in an intranuclear cascade. Increasing τ_0 then increases the fraction of QEL events with a low momentum proton and thus populates the 1-track sample to the detriment of the 2-track sample. This is the reason for the systematic overestimation of M_A extracted from the 1-track sample alone and its underestimation when extracted from the 2-track sample alone. However the value of M_A extracted from the combination of the 1-track and 2-track samples is almost insensitive to variations of the τ_0 parameter.

We also find that using the QEL Monte Carlo with $\tau_0 = 1$ and $\alpha^F_{\rm mod} = 0.6$ provides the most accurate prediction for the ratio between the 1-track and 2-track samples (and hence the most adequate description of the FSI interactions): in this

Table 7. Parameters of the QEL MC simulation (axial mass $M_A^{\rm mc}$ and parameters of FSI modeling) are listed in the first three columns. The intermediate columns contain results of the QEL ν_μ cross-section measurement (in units of 10^{-38} cm^2, without errors) for the different topology of identified events. The axial mass value obtained from the fit of Q^2 distribution and $\sigma \otimes d\sigma/dQ^2$ fit ($Q^2_{\rm lim} = 0.2 - 4$ GeV^2) are given in the last columns of the table; the given axial mass errors δM_A are from MINUIT output

MC parameters			Single track		Two tracks		Combined		Fit of Q^2 distribution			Fit of $\sigma \otimes d\sigma/dQ^2$		
τ_0	$\alpha^F_{\rm mod}$	$M_A^{\rm mc}$	$\sigma_{\rm qel}$	M_A	$\sigma_{\rm qel}$	M_A	$\sigma_{\rm qel}$	M_A	$M_A \pm \delta M_A$		χ^2	$M_A \pm \delta M_A$		χ^2
NUANCE FSI		1.03	0.888	1.018	0.963	1.097	0.915	1.047	1.077	0.061	14.9	1.098	0.018	14.9
0.60	0.60	0.83	0.863	0.990	1.014	1.148	0.915	1.047	1.113	0.057	19.4	1.105	0.018	19.3
1.00	0.60	0.83	0.885	1.015	0.956	1.090	0.912	1.043	1.095	0.057	11.6	1.058	0.018	11.9
2.00	0.60	0.83	0.918	1.050	0.851	0.977	0.892	1.021	0.960	0.093	17.4	0.965	0.018	17.4
0.60	0.60	0.93	0.882	1.011	1.015	1.148	0.928	1.061	1.135	0.056	10.0	1.119	0.018	10.0
1.00	0.60	0.93	0.893	1.023	0.942	1.074	0.911	1.043	1.075	0.060	13.5	1.065	0.018	13.5
2.00	0.60	0.93	0.931	1.063	0.844	0.968	0.896	1.026	1.009	0.069	12.2	0.971	0.018	12.4
0.60	0.60	1.03	0.910	1.041	0.977	1.110	0.935	1.067	1.016	0.051	25.8	1.094	0.017	27.1
1.00	*0.60*	*1.03*	*0.919*	*1.051*	*0.918*	*1.050*	*0.919*	*1.051*	*1.073*	*0.059*	*18.7*	*1.059*	*0.018*	*18.7*
2.00	0.60	1.03	0.950	1.083	0.819	0.939	0.896	1.026	0.993	0.079	18.4	0.968	0.018	18.4
0.60	0.60	1.13	0.946	1.079	0.979	1.113	0.959	1.092	1.031	0.077	24.9	1.109	0.017	26.4
0.80	0.60	1.13	0.948	1.081	0.926	1.058	0.940	1.073	1.092	0.056	13.8	1.079	0.018	13.8
1.00	0.60	1.13	0.962	1.096	0.904	1.035	0.940	1.072	1.100	0.062	19.4	1.060	0.018	19.6
2.00	0.60	1.13	0.995	1.129	0.789	0.904	0.906	1.037	0.999	0.080	18.0	0.956	0.018	18.2
0.60	0.60	1.23	0.994	1.127	0.925	1.058	0.967	1.100	1.039	0.053	20.7	1.088	0.018	21.2
0.80	0.60	1.23	0.996	1.129	0.904	1.035	0.959	1.092	1.013	0.039	21.1	1.066	0.017	21.7
1.00	0.60	1.23	1.000	1.134	0.879	1.008	0.951	1.085	0.970	0.087	20.1	1.051	0.017	21.3
2.00	0.60	1.23	1.038	1.171	0.777	0.889	0.921	1.053	0.996	0.079	20.9	0.964	0.018	16.3
0.80	0.54	1.03	0.921	1.053	0.963	1.097	0.937	1.070	1.113	0.054	20.9	1.079	0.018	21.1
0.80	0.57	1.03	0.921	1.052	0.950	1.083	0.932	1.064	1.072	0.062	15.5	1.067	0.018	15.5
0.80	0.60	1.03	0.920	1.051	0.959	1.092	0.935	1.067	1.090	0.064	12.7	1.089	0.018	12.7
0.80	0.63	1.03	0.912	1.044	0.953	1.087	0.928	1.060	1.082	0.062	15.8	1.084	0.018	15.7
0.80	0.66	1.03	0.905	1.035	0.933	1.066	0.916	1.047	0.989	0.091	19.9	1.067	0.017	20.9
0.80	0.69	1.03	0.904	1.035	0.940	1.072	0.918	1.049	0.937	0.113	15.7	1.070	0.017	18.0

case the flux averaged QEL cross section stays approximately the same whether measured from the 1-track sample or from the 2-track sample. This allows us to exclude the MC sets with $\tau_0 = 0.6$ and 2.0 from further considerations.

Similarly we have observed that when using the full sample (1-track and 2-track) the measured M_A is not very sensitive to modifications of the $\alpha^F_{\rm mod}$ parameter. And using the NUANCE simulation code as a cross check gives a very consistent picture: the M_A value extracted from the 1-track sample is also different from the one extracted from the 2-track sample, while the value obtained with the combined sample nicely agrees with our measurement with the best FSI parameters. Thus, our results for the neutrino case are:

$$\begin{aligned} \langle\sigma_{\rm qel}\rangle_{\nu_\mu} &= (0.92 \pm 0.02\ ({\rm stat.})\ \pm 0.06\ ({\rm syst.}))\ \cdot 10^{-38}\ {\rm cm}^2, \\ M_A &= 1.05 \pm 0.02\ ({\rm stat.})\ \pm 0.06\ ({\rm syst.})\ {\rm GeV}. \end{aligned} \tag{25}$$

This result (25) is indeed in agreement with both the standard fit of the Q^2 distribution and the fit of the combined $\sigma \otimes d\sigma/dQ^2$ distribution of the NOMAD data:

$$M_A = 1.06 \pm 0.02\ ({\rm stat.})\ \pm 0.06\ ({\rm syst.})\ {\rm GeV} \tag{26}$$

(this result is obtained with a QEL MC using $M_A = 1.03$ GeV).

We use the 2-track sample only to extract M_A from the fit of the Q^2 distribution since in this case the purity of QEL identification is rather high ($\sim 74\%$, see Table 4).

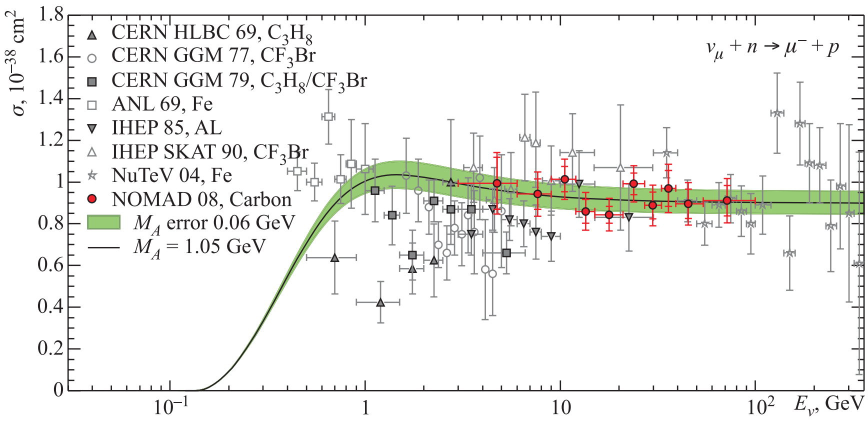

Fig. 17. Comparison of our measurements with the previous experimental data from Fig. 2. The solid line and error band correspond to the M_A value obtained in the NOMAD experiment. Nuclear effects are included into calculations according to the standard relativistic Fermi gas model. The theoretical band corresponds to both statistical and systematic uncertainties

The results depend on the input MC parameters (axial mass and formation time) but still are in nice agreement with the results of the extraction of M_A from the measured QEL cross section based also on a 2-track sample analysis. This can be considered as an additional confidence for our measurements using the full QEL sample.

The measured cross section of the $\nu_\mu n \to \mu^- p$ reaction as a function of the neutrino energy is shown in Figs. 17 and 18. These results are compared to the previous measurements performed with deuterium and heavy nuclei targets.

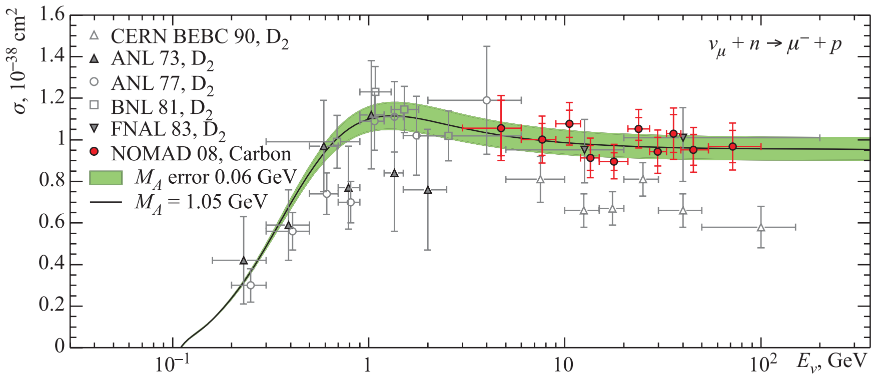

Fig. 18. Comparison of our measurements with the previous experimental data from Fig. 1. The solid line and error band correspond to the M_A value obtained in the NOMAD experiment. All experimental data are corrected for nuclear effects

8.2. $\bar{\nu}_\mu p \to \mu^+ n$ Sample. Since our measurement of the cross section of the $\bar{\nu}_\mu p \to \mu^+ n$ reaction is based on the 1-track sample only, we do not show the dependence of the results on the variation of the τ_0 and $\alpha^F_{\rm mod}$ parameters. Instead we display a dependence on the input M_A in Table 8. The results for the measured M_A are found to be quite stable. In Fig. 19 we show the measured $\bar{\nu}_\mu p \to \mu^+ n$ cross section as a function of the antineutrino energy superimposed with the theoretical curve drawn with $M_A = 1.06 \pm 0.12$ GeV and with nuclear effects according to the standard relativistic Fermi gas model. Table 8 summarizes our results for the $\bar{\nu}_\mu p \to \mu^+ n$ cross-section measurement in the different antineutrino energy intervals. The cross sections are measured on a carbon target and also recalculated for a free nucleon. The statistical and systematic errors are both provided. The observed number of events in the data, the predicted number of background events, the background subtracted and efficiency corrected number of events are also shown.

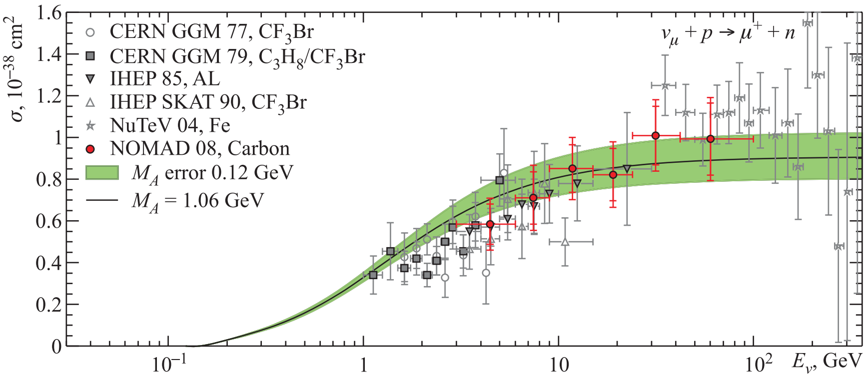

Fig. 19. Comparison of our measurements with the previous experimental data from Fig. 3. The solid line and error band correspond to the M_A value obtained in the NOMAD experiment. Nuclear effects are included into calculations according to the standard relativistic Fermi gas model. The theoretical band corresponds to both statistical and systematic uncertainties

Our final results for the antineutrino case are:

$$\begin{aligned} \langle\sigma_{\rm qel}\rangle_{\bar{\nu}_\mu} &= (0.81 \pm 0.05\ (\text{stat.})\ \pm 0.08\ (\text{syst.}))\ \cdot 10^{-38}\ \text{cm}^2, \\ M_A &= 1.06 \pm 0.07\ (\text{stat.})\ \pm 0.10\ (\text{syst.})\ \text{GeV}. \end{aligned} \tag{27}$$

9. CONCLUSIONS

The cross-section measurement of the $\nu_\mu n \to \mu^- p$ and $\bar{\nu}_\mu p \to \mu^+ n$ reactions on nuclear target was performed and reported in this paper. The samples used in the analysis consist of 14021 neutrino and 2237 antineutrino events, which were identified as quasi-elastic neutrino scattering among the experimental data collected by the NOMAD collaboration.

We have discussed in detail the analysis procedure and the most significant sources of systematic error. Special attention was paid to the influence of the FSI effects on the measured physical quantities. The DPMJET code was used to simulate these FSI effects. We also proposed a method for tuning the intranuclear cascade parameters (mainly the formation time τ_0), which was then used to reduce the corresponding systematic uncertainty.

For the ν_μ case stable results have been obtained with the combined 1-track and 2-track samples since they are almost insensitive to the FSI effects.

The results for the flux averaged QEL cross sections in the (anti)neutrino energy interval 3–100 GeV are $\langle\sigma_{\rm qel}\rangle_{\nu_\mu} = (0.92 \pm 0.02\ (\text{stat.}) \pm 0.06\ (\text{syst.})) \cdot 10^{-38}\ \text{cm}^2$ and $\langle\sigma_{\rm qel}\rangle_{\bar{\nu}_\mu} = (0.81 \pm 0.05\ (\text{stat.}) \pm 0.08\ (\text{syst.})) \cdot 10^{-38}\ \text{cm}^2$ for

Table 8. The results of QEL $\bar{\nu}_\mu$ cross-section measurement. The parameters of the DPMJET model are $\tau_0 = 0.8$, $\alpha^F_{\mathbf{mod}} = 0.6$

$M_A^{\rm mc}$	$\sigma_{\rm qel}$	M_A
0.83	0.794	1.042
0.93	0.799	1.048
1.03	*0.811*	*1.063*
1.13	0.834	1.094
1.23	0.861	1.127

neutrino and antineutrino, respectively. The axial mass M_A was calculated from the measured cross sections: we find $M_A = 1.05 \pm 0.06$ GeV from the ν_μ sample and $M_A = 1.06 \pm 0.12$ GeV from the $\bar{\nu}_\mu$ sample. The M_A parameter was also extracted from the fit of the Q^2 distribution in the high purity sample of ν_μ quasi-elastic 2-track events (with a reconstructed proton track). It was found to be consistent with the values calculated from the cross sections.

Our results are in agreement with the existing world average value [32,35] and do not support the results found in the recent measurements from the NuTeV [23], K2K [24,25] and MiniBooNE [26] collaborations, which reported somewhat larger values, however still compatible with our results within their large errors.

It should also be noted that the preliminary results reported earlier by the NOMAD collaboration for the 2-track sample only [79, 80] suffered from a large systematic bias related to an improper treatment of the FSI effects in the simulation program. Now they should be superseeded by the new measurements reported here.

Acknowledgements. We gratefully acknowledge the CERN SPS accelerator and beam-line staff for the magnificent performance of the neutrino beam during the data taking period of the NOMAD experiment. We would like to thank all our colleagues from the NOMAD collaboration for their crucial contribution to the data taking and analysis presented in this work. Our special thanks to the members of the LPHNE(Paris)-NOMAD group (Pierre Astier, Jacques Dumarchez, Antoine Letessier-Selvon, Jean-Michel Levy, Kyan Schahmaneche and Francois Vannucci) as well as to S. A. Bunyatov, Luigi Di Lella, Leslie Loris Camilleri, Mauro Mezzetto, Roberto Petti and Sanjib Mishra for fruitful discussions and critical comments. We acknowledge contributions of D. V. Naumov at the early stage of the analysis described here. Special thanks for useful discussions of theoretical issues go to K. Kuzmin and V. Naumov. We are grateful to J. Ranft for the important explanations and technical assistance with the DPMJET code. V. Lyubushkin is very grateful to the LPNHE (Paris) for the warm hospitality and financial support during the final stage of this work.

This work was supported by the Russian Foundation for Basic Research (grant 08-02-00018).

REFERENCES

1. *Kustom R. L., Lundquist D. E., Novey T. B., Yokosawa A., Chilton F.* // Phys. Rev. Lett. 1969. V. 22. P. 1014.
2. *Mann W. A. et al.* // Phys. Rev. Lett. 1973. V. 31. P. 844.
3. *Barish S. J. et al.* // Phys. Rev. D. 1977. V. 16. P. 3103.
4. *Miller K. L. et al.* // Phys. Rev. D. 1982. V. 26. P. 537.
5. *Fanourakis G. et al.* // Phys. Rev. D. 1980. V. 21. P. 562.
6. *Baker N. J. et al.* // Phys. Rev. D. 1981. V. 23. P. 2499.
7. *Ahrens L. A. et al.* // Phys. Lett. B. 1988. V. 202. P. 284.
8. *Kitagaki T. et al.* // Phys. Rev. D. 1990. V. 42. P. 1331.
9. *Kitagaki T. et al.* // Phys. Rev. D. 1983. V. 28. P. 436.
10. *Asratian A. E. et al.* // Phys. Lett. B. 1984. V. 137. P. 122.
11. *Block M. M. et al.* // Phys. Lett. 1964. V. 12. P. 281.
12. *Orkin-Lecourtois A. et al.* // Nuovo Cim. A. 1967. V. 50. P. 927.
13. *Holder M. et al.* // Nuovo Cim. A. 1968. V. 57. P. 338.
14. *Budagov I. et al.* // Lett. Nuovo Cim. 1969. V. 2. P. 689.
15. *Bonetti S. et al.* // Nuovo Cim. A. 1977. V. 38. P. 260.
16. *Armenise N. et al.* // Nucl. Phys. B. 1979. V. 152. P. 365.
17. *Pohl M. et al.* // Lett. Nuovo Cim. 1979. V. 26. P. 332.
18. *Allasia D. et al.* // Nucl. Phys. B. 1990. V. 343. P. 285.
19. *Belikov S. V. et al.* // Yad. Fiz. 1982. V. 35. P. 59.
20. *Belikov S. V. et al.* // Z. Phys. A. 1985. V. 320. P. 625.
21. *Grabosch H. J. et al.* // Sov. J. Nucl. Phys. 1988. V. 47. P. 1032.
22. *Brunner J. et al.* // Z. Phys. C. 1990. V. 45. P. 551.
23. *Suwonjandee N.* Ph. D. Thesis. University of Cincinnati, 2004.
24. *Gran R. et al. (K2K Collab.)* // Phys. Rev. D. 2006. V. 74. P. 052002; hep-ex/0603034
25. *Mariani C. (K2K Collab.)* // AIP Conf. Proc. 2008. V. 981. P. 247.

26. *Aguilar-Arevalo A. A. et al. (MiniBooNE Collab.)* // Phys. Rev. Lett. 2008. V. 100. P. 032301; hep-ex/0706.0926

27. *Aguilar-Arevalo A. A. et al. (SciBooNE Collab.).* hep-ex/0601022, 2006.

28. *Drakoulakos D. et al. (Minerva Collab.).* hep-ex/0405002. 2004.

29. *Altegoer J. et al. (NOMAD Collab.)* // Nucl. Instr. Meth. A. 1998. V. 404. P. 96.

30. *Astier P. et al. (NOMAD Collab.)* // Nucl. Instr. Meth. A. 2003. V. 515. P. 800; hep-ex/0306022

31. *Smith R. A., Moniz E. J.* // Nucl. Phys. B. 1972. V. 43. P. 605.

32. *Bernard V., Elouadrhiri L., Meissner U.G.* // J. Phys. G. 2002. V. 28. P. R1; hep-ph/0107088

33. *Budd H., Bodek A., Arrington J.* hep-ex/0308005. 2003.

34. *Budd H., Bodek A., Arrington J.* // Nucl. Phys. Proc. Suppl. 2005. V. 139. P. 90; hep-ex/0410055

35. *Bodek A., Avvakumov S., Bradford R., Budd H.* // Eur. Phys. J. C. 2008. V. 53. P. 349; hep-ex/0708.1946

36. *Anfreville M. et al.* // Nucl. Instr. Meth. A. 2002. V. 481. P. 339; hep-ex/0104012

37. *Bassompierre G. et al.* // Nucl. Instr. Meth. A. 1998. V. 403. P. 363.

38. *Bassompierre G. et al.* // Nucl. Instr. Meth. A. 1998. V. 411. P. 63.

39. *Autiero D. et al.* // Nucl. Instr. Meth. A. 1996. V. 373. P. 358.

40. *Autiero D. et al.* // Nucl. Instr. Meth. A. 1998. V. 411. P. 285.

41. *Astier P. et al. (NOMAD Collab.)* // Nucl. Phys. B. 2001. V. 611. P. 3; hep-ex/0106102

42. *Astier P. et al. (NOMAD Collab.)* // Phys. Lett. B. 2003. V. 570. P. 19; hep-ex/0306037

43. *Llewellyn Smith C. H.* // Phys. Rep. 1972. V. 3. P. 261.

44. *Gari M. F., Kruempelmann W.* // Phys. Lett. B. 1992. V. 274. P. 159.

45. *Lomon E. L.* // Phys. Rev. C. 2002. V. 66. P. 045501; nucl-th/0203081

46. *Lomon E. L.* nucl-th/0609020. 2006.

47. *Eidelman S. et al. (Particle Data Group)* // Phys. Lett. B. 2004. V. 592. P. 1.

48. *Rein D., Sehgal L. M.* // Ann. Phys. 1981. V. 133. P. 79.

49. *Rein D.* // Z. Phys. C. 1987. V. 35. P. 43.

50. *Kuzmin K. S., Lyubushkin V. V., Naumov V. A.* // Mod. Phys. Lett. A. 2004. V. 19. P. 2815; hep-ph/0312107

51. *Kuzmin K. S., Lyubushkin V. V., Naumov V. A.* // Nucl. Phys. Proc. Suppl. 2005. V. 139. P. 158; hep-ph/0408106

52. *Feynman R. P., Kislinger M., Ravndal F.* // Phys. Rev. D. 1971. V. 3. P. 2706.

53. *Furuno K. et al.* // 2nd Intern. Workshop on Neutrino–Nucleus Interactions in the Few GeV Region. NUINT 02., Irvine, California, December 12–15, 2002.

54. *Kuzmin K. S., Lyubushkin V. V., Naumov V. A.* hep-ph/0511308. 2005.

55. *Ingelman G., Edin A., Rathsman J.* // Comp. Phys. Commun. 1997. V. 101. P. 108; hep-ph/9605286

56. *Levy J. M.* hep-ph/0407371. 2004.

57. *Ellis J. R., Kotzinian A., Naumov D. V.* // Eur. Phys. J. C. 2002. V. 25. P. 603; hep-ph/0204206

58. *Sjostrand T.* hep-ph/9508391. 1995.

59. *Sjostrand T.* // Comp. Phys. Commun. 1986. V. 39. P. 347.

60. *Sjostrand T., Bengtsson M.* // Comp. Phys. Commun. 1987. V. 43. P. 367.

61. *Melnitchouk W., Ent R., Keppel C.* // Phys. Rep. 2005. V. 406. P. 127; hep-ph/0501217

62. *Graczyk K. M., Juszczak C., Sobczyk J. T.* // Nucl. Phys. A. 2007. V. 781. P. 227; hep-ph/0512015

63. *Andreopoulos C. (GENIE)* // Acta Phys. Polon. B. 2006. V. 37. P. 2349.

64. *Kuzmin K. S., Lyubushkin V. V., Naumov V. A.* // Phys. At. Nucl. 2006. V. 69. P. 1857.

65. *L. J. Winton.* Ph D Thesis. University of Melbourne, 1999.

66. *Rein D., Sehgal L. M.* // Nucl. Phys. B. 1983. V. 223. P. 29.

67. *Rein D.* // Nucl. Phys. B. 1986. V. 278. P. 61.

68. *Benhar O., Fabrocini A., Fantoni S., Sick I.* // Nucl. Phys. A. 1994. V. 579. P. 493.

69. *Kulagin S. A., Petti R.* // Nucl. Phys. A. 2006. V. 765. P. 126; hep-ph/0412425

70. *Battistoni G., Lipari P., Ranft J., Scapparone E.* hep-ph/9801426. 1998.

71. *Ranft J.* // Z. Phys. C. 1989. V. 43. P. 439;
Ferrari A., Sala P. R., Ranft J., Roesler S. // Z. Phys. C. 1996. V. 70. P. 413; nucl-th/9509039

72. *Casper D.* // Nucl. Phys. Proc. Suppl. 2002. V. 112. P. 161; hep-ph/0208030

73. *Paschos E. A., Yu J. Y., Sakuda M.* // Phys. Rev. D. 2004. V. 69. P. 014013; hep-ph/0308130

74. *Marchionni A., Veltri M.* (NOMAD Collab.). Internal Memo 98–023. 1998.

75. *Yabsley B. D.* (NOMAD Collab.). Internal Memo 97–028. 1997.

76. *Yabsley B. D.* (NOMAD Collab.). Internal Memo 98–011. 1998.

77. *Kayis-Topaksu A. et al.* // Eur. Phys. J. C. 2003. V. 30. P. 159.

78. *Vilain P. et al.* // Phys. Lett. B. 1995. V. 364. P. 121.

79. *Petti R.* (NOMAD Collab.). hep-ex/0411032. 2004.

80. *Lyubushkin V. V., Popov B. A.* // Phys. At. Nucl. 2006. V. 69. P. 1876.

Received on July 18, 2008.

Корректор *Т. Е. Попеко*

Подписано в печать 18.11.2008.
Формат 60 × 90/16. Бумага офсетная. Печать офсетная.
Усл. печ. л. 2,75. Уч.-изд. л. 3,87. Тираж 365 экз. Заказ № 56404.

Издательский отдел Объединенного института ядерных исследований
141980, г. Дубна, Московская обл., ул. Жолио-Кюри, 6.
E-mail: publish@jinr.ru
www.jinr.ru/publish/